Smart digital control of superconducting quantum interference devices for ultra-low-field magnetic resonance imaging

Antti Mäkinen

School of Science

Thesis submitted for examination for the degree of Master of Science in Technology

Espoo 24.11.2015

Thesis supervisor:

Prof. Risto Ilmoniemi

Thesis advisor:

Koos Zevenhoven, M.Sc.

Aalto University
School of Science

AALTO UNIVERSITY
SCHOOL OF SCIENCE

ABSTRACT OF THE
MASTER'S THESIS

Author: Antti Mäkinen

Title: Smart digital control of superconducting quantum interference devices for ultra-low-field magnetic resonance imaging

Date: 24.11.2015 Language: English Number of pages: 8+51

Department of Neuroscience and Biomedical Engineering

Professorship: Biomedical Engineering

Supervisor: Prof. Risto Ilmoniemi

Advisor: Koos Zevenhoven, M.Sc.

Ultra-low-field magnetic resonance imaging (ULF MRI) studies the inner structure of matter by exciting nuclear spins using microtesla-range magnetic fields. The weak spin-induced magnetic signals are received with highly sensitive superconducting-quantum-interference-device-based (SQUID) sensors that act as flux-to-voltage converters. Because of the physical nature of the SQUID, its response to magnetic flux is periodic. To make the measurements easier, the response is linearized with a special feedback scheme.

In the measurement setup used in this work, the SQUID feedback is realized with digital signal processors so that the response of the system can be manipulated using computer software. The software is designed for magnetoencephalography, which measures magnetic signals generated by the neuronal currents. These signals are in both amplitude and frequency smaller than those encountered in ULF MRI.

In this thesis, new software for the needs of ULF MRI was developed. For example, a method to measure the feedback-to-input response and a new feedback reset algorithm tailored for ULF MRI were designed and implemented. The reset algorithm was designed to reactivate the flux dams in the SQUID input circuits and to reduce the signal transient after the reset. The feedback-to-input response measurements revealed a notable delay in the feedback, which degrades the frequency response of the whole system. It was shown that the frequency response can be improved by an additional digital compensation based on the measured feedback-to-input response.

Keywords: SQUID, ULF MRI, digital, flux-locked loop, reset, frequency response

AALTO-YLIOPISTO
PERUSTIETEIDEN KORKEAKOULU

DIPLOMITYÖN
TIIVISTELMÄ

Tekijä: Antti Mäkinen

Työn nimi: Suprajohtavien kvantti-inferferenssilaitteiden älykäs digitaalinen ohjaus ultramatalan kentän magneettikuvauksessa

Päivämäärä: 24.11.2015 Kieli: Englanti Sivumäärä: 8+51

Neurotieteen ja lääketieteellisen tekniikan laitos

Professuuri: Lääketieteellinen tekniikka

Työn valvoja: Prof. Risto Ilmoniemi

Työn ohjaaja: DI Koos Zevenhoven

Ultramatalan kentän magneettikuvauksessa tutkitaan aineen rakennetta virittämällä atomiytimien spinejä mikroteslaluokan magneettikentillä. Spinien tuottamat heikot magneettiset signaalit vastaanotetaan erittäin herkillä suprajohtaviin kvantti-interferenssilaitteisiin (SQUID) perustuvilla antureilla, jotka muuntavat magneettivuon jännitteeksi. SQUIDin vaste magneettivuohon on luonnostaan periodinen. Mittausten helpottamiseksi se linearisoidaan kytkemällä mitattu signaali takaisin SQUIDiin.

Tässä työssä käytetyssä mittausjärjestelmässä SQUIDien takaisinkytkentä on toteutettu digitaalisten signaaliprosessoreiden avulla, minkä ansiosta systeemin vastetta voidaan muokata tietokoneohjelmistolla. Ohjelmisto on kuitenkin suunniteltu magnetoenkefalografiaa varten. Magnetoenkefalografiassa mitatut signaalit ovat niin taajuudeltaan kuin amplitudiltaan huomattavan pieniä verattuna magneettikuvaukseen.

Tämän diplomityön tarkoituksena oli kehittää uutta ohjelmistoa ultramatalan kentän magneettikuvauksen tarpeisiin. Ohjelmistoa kehitettiin esimerkiksi mittaamaan takaisinkytkentävasteita sekä kontrolloimaan vuosignaalia uudella tavalla takaisinkytkennän resetoinnin aikana. Uusi resetointialgoritmi pyrkii ohjaamaan SQUIDien vastaanottopiirien vuopatoja suprajohtavaan tilaan sekä vähentämään signaalitransienttia takaisinkytkennän resetoinnin jälkeen. Takaisinkytkennässä havaittiin viivettä, joka heikentää koko systeemin taajuusvastetta. Taajuusvasteen osoitettiin kohentuvan, kun signaalia kompensoitiin digitaalisesti hyödyntäen tietoa mitatusta takaisinkytkentävasteesta.

Avainsanat: SQUID, ULF MRI, digitaalinen, vuolukittu silmukka, resetointi, taajuusvaste

Preface

I clearly remember when my interested in mathematics and physics really sprang up. My teacher in the small upper secondary school of Mänttä organized a special course on mathematical physics, where we derived, for instance, the ideal gas law from the motion of gas molecules. On that course, I realized that mathematics is a powerful tool for solving many kinds of problems. After that, I decided to apply to study engineering physics at Helsinki University of Technology, which then became part of Aalto University before the beginning of my studies.

I began my work in the MEGMRI group in the Department of Neuroscience and Biomedical Engineering as a summer student in 2013. During this time, the department has also changed its name, but my motivation for learning and understanding new things has not changed a bit. These five years at Aalto University with the two and a half years in this research group have been the most demanding but also the most rewarding period of my life.

This master's thesis project has been a really instructive experience, too. First, I wish to thank my supervisor professor Risto Ilmoniemi who has made it possible for me to work in this group. Second, many thanks to my advisor Koos Zevenhoven. He knows a great deal about ultra-low-field MRI among many other things and has been a big help when solving problems and writing this thesis. I also thank the other group members and summer students in the MEGMRI group who have been pleasant to work with. Special thanks to professor Lauri Parkkonen who has shared his knowledge of the specific features in the measurement system. Thanks to Joonas Iivanainen for motivating discussions and for sharing the same office.

My time at Aalto University would not have been the same without my friends and the people in the Guild of Physics. The Physicist Spex has motivated me to practice dancing and introduced me to new people coming also from other fields than physics. So, thanks to all of you who had organized events till late night, solved exercise problems at Kiltis, played badminton in Otahalli, or otherwise had fun with me. Finally, thanks to Viivi who has supported me and listened to my endless chatter about math stuff.

Otaniemi, 24.11.2015

Antti Mäkinen

Contents

Symbols and abbreviations

Symbols

F	Frequency
F_s	Sampling frequency
Ω	Angular frequency
ω	Normalized angular frequency
t	Time
n	Time index
$x[n]$	Input signal
$y[n]$	Output signal
$h[n]$	Impulse response
$H(z)$	Transfer function
$H_{\mathrm{fb}\to\mathrm{in}}(z)$	Feedback-to-input transfer function
Φ_{in}	Measured magnetic flux as seen by the SQUID
Φ_{fb}	Feedback magnetic flux as seen by the SQUID
Φ_{tot}	Total magnetic flux as seen by the SQUID
Φ_0	Magnetic flux quantum
V_Φ	SQUID flux-to-voltage transfer coefficient
$\vec{B}_0$	Static measurement field in NMR and MRI
$\vec{B}_{\mathrm{p}}$	Prepolarizing field in NMR and MRI

Abbreviations

AC	Alternating (current)
A/D	Analog to digital
ADC	Analog-to-digital converter
D/A	Digital to analog
DAC	Digital-to-analog converter
DC	Direct (current)
DFII	Direct form II
DSP	Digital signal processor
FIR	Finite impulse response
FLL	Flux-locked loop
IIR	Infinite Impulse response
LTI	Linear and time-invariant
MEG	Magnetoencephalography
MRI	Magnetic resonance imaging
NMR	Nuclear magnetic resonance
SQUID	Superconducting quantum interference device
SNR	Signal-to-noise ratio
ULF MRI	Ultra-low-field magnetic resonance imaging

Operators

a^*	Complex conjugate of a
$\oint$	Closed path integral
∇	Spatial gradient
$\frac{d}{dt}$	Time derivative
Re	Real part
Im	Imaginary part
$\vec{a} \cdot \vec{b}$	Dot product of $\vec{a}$ and $\vec{b}$
$a * b$	Convolution of a and b
$\texttt{atan2}(y, x)$	Two-argument arctangent; angle corresponding to (y, x)

1 Introduction

Magnetic resonance imaging (MRI) studies non-invasively the inner structure of matter by imaging the spins of hydrogen nuclei with the help of magnetic fields [1, 2]. It is a technology widely used in medical diagnosis thanks to its soft-tissue contrast and safety compared to ionizing techniques, such as x-ray computed tomography. Traditionally, high magnetic fields have been favored in imaging, since they provide better image quality. Nonetheless, there has been also interest in developing devices that operate with lower fields, even in the range of microteslas [3]. This approach is usually called ultra-low-field (ULF) MRI.

In ultra-low-field studies, the spin-induced signals are usually recorded using sensors based on *superconducting quantum interference devices* (SQUIDs), which offer superior sensitivity over the usual Faraday detection. A SQUID is a superconducting ring interrupted with two insulating junctions. Due to quantum-mechanical phenomena, the sum of the currents through these junctions depends periodically on the magnetic flux applied on the sensor loop.

Another imaging method that exploits SQUID sensors is *magnetoencephalography* (MEG), which non-invasively measures the magnetic fields generated by the neuronal currents in the cerebral cortex [4]. The magnetic field around the head gives information about the activity of different brain areas, and thus MEG is suited for functional brain studies. ULF MRI can be made compatible with MEG by using the same sensors for both modalities. A hydrid MEG–MRI system enables the study of brain structure and function using only one device, which can significantly simplify the workflow of MEG studies.

The aim of this thesis is to study the digital control of SQUID sensors in an MEG–MRI device, but mainly focusing on the requirements of ULF MRI. The response of a SQUID to the applied flux is highly non-linear. In order to linearize the response, a feedback scheme called the *flux-locked loop* (FLL) is used [5]. As the name suggests, the total flux through the SQUID is kept constant using the feedback signal that equals the applied flux up to a constant. In the Aalto MEG–MRI device [6], which is based on a commercial MEG system, the feedback is implemented digitally, in software, using *digital signal processors* (DSPs).

ULF MRI sequences use relatively strong magnetic pulses, which disturb the operation of the SQUID sensors. The fields are so large that the feedback cannot keep track of the applied flux. To restore the operation of the feedback system, the feedback signals are nulled, or reset, before the signal acquisition. The suboptimal behavior of the feedback system and transients from the digital signal processing lead to disturbances in the final readout long after the reset. This work addresses those problems by introducing a new algorithm for the initialization of signal acquisition.

Another task, in this work, was to study the frequency response of the closed-loop system. For this purpose, the flux-locked loop was modeled as a discrete-time system, and different parts of it were measured using new software methods implemented on the DSP units. The measurement hardware is not necessarily optimal for measuring frequencies higher than a few kHz using the ordinary methods. It was, however, studied how the frequency response can be improved by compensating hardware

non-idealities within the software.

Sec. 2 provides a theoretical background to ULF MRI, SQUID sensors, and digital signal processing. Then, in Sec. 3, the measurement system, the feedback loop model and new software methods are introduced. Sec. 4 describes the results of the measurements of the feedback system properties as well as the feedback reset. Sec. 5 summarizes the results and concludes the work.

2 Background

2.1 Ultra-low-field magnetic resonance imaging

In this section, I review some of the basics of MRI, proceeding to imaging at ultra-low fields using SQUID sensors. The physical theory and reconstruction principles of MRI are discussed in textbooks, e.g., Refs. [1, 2]. A good review of SQUID-detected MRI can be found in Ref. [3]. At the end of this section, I explain how ULF MRI is combined with MEG and what benefits the combination can offer.

2.1.1 MRI basics

MRI is an imaging technique where the hydrogen nuclei, i.e., protons of an imaged volume are excited and measured using the principles of *nuclear magnetic resonance* (NMR). The proton possesses an internal angular momentum, called spin, which creates a tiny magnetic moment for the particle. When an external *measurement field* $\vec{B}_0$ is applied to the volume, the proton energy depends on the spin orientation. The quantum mechanical state of the particle can be expressed as a linear combination of the Hamiltonian eigenstates that correspond to the spin parallel (lower energy) and anti-parallel (higher energy) to $\vec{B}_0$. The energy difference between the eigenstates is

$$\Delta E = \hbar \gamma B_0 \,, \tag{1}$$

where $\hbar$ is the reduced Planck constant and γ the proton gyromagnetic ratio. Because of the lower energy, the probability of finding a spin parallel to $\vec{B}_0$ exceeds that of the anti-parallel spin. However, at room temperature, $T \approx 300$ K, the thermal energy is much greater than ΔE, making the energetic benefit less significant, thus leveling the probabilities. The average of the states in the whole spin ensemble determines the equilibrium magnetization, which, in the high-temperature limit ($\Delta E \ll k_\mathrm{B} T$), is given by [1]

$$M_0(T) = \frac{\Delta E}{2 k_\mathrm{B} T} M_0(0\ \mathrm{K}) \,, \tag{2}$$

where k_B is the Boltzmann constant and $M_0(0\,\mathrm{K})$ the magnetization created by all spins in the parallel state. At room temperature, for a field around 1 T, the ratio $M_0(300\ \mathrm{K})/M_0(0\ \mathrm{K})$ is only a few parts in a million, which fortunately is enough to create measurable signals.

The measurement conditions are always noisy, and hence the static magnetic field originating from the magnetization is extremely difficult to measure. The magnetization can, however, be manipulated with the help of the phenomenological Bloch equation [1],

$$\frac{d\vec{M}}{dt} = \gamma \vec{M} \times \vec{B} - \frac{\vec{M}_\perp}{T_2} - \frac{\vec{M}_z - \vec{M}_0}{T_1} \,, \tag{3}$$

where $\vec{B}$ is the total magnetic field, $\vec{M}_\perp$ the part of the magnetization perpendicular to $\vec{B}_0$, $\vec{M}_z$ the part parallel to $\vec{B}_0$, and T_1 and T_2 are relaxation time constants. According to this equation, a short pulse of circularly polarized oscillating magnetic

field can tip the magnetization by 90° from the direction of $\vec{B}_0$. After that, the magnetization starts to precess around $\vec{B}_0$ at angular frequency $\Omega_0 = \gamma B_0$, commonly known as the *Larmor frequency*. The precessing magnetization yields an oscillating magnetic signal, which can be measured, for example, by Faraday induction. Since the Larmor frequency depends on the measurement field magnitude B_0, that magnitude sets requirement for the frequency response of the measurement system.

By spatially varying the Larmor frequency of the precessing spins, some spatial information can be encoded in the NMR signals, which can be then used for imaging. This is accomplished with a special gradient coil by linearly varying the z component of the magnetic field during the measurement, for example, along the x direction. The rest of the spatial information can be encoded in the signal phase by applying gradients before the measurement. When such a phase gradient varies along the y direction, the frequency and phase, after applying the phase-encoding pulse, can be written as

$$\Omega(x) = \gamma(B_0 + G_x x) \quad \text{and} \quad \phi(y) = \gamma(B_0 + G_y y)\tau\,, \tag{4}$$

where $G_x x$ and $G_y y$ are the magnitudes of the linear gradient fields and τ is the duration of the phase gradient pulse. For three-dimensional imaging, also the z direction is phase-encoded. Combining these encoding methods in a systematic fashion in multiple measurement sequences, the data for the MR image can be acquired. A schematic illustration of the gradients in a ULF MRI sequence is shown in Fig. 1.

Different tissue types can be distinguished by their specific proton densities but also by their specific relaxation time constants T_1 and T_2 introduced in Eq. (3). The *longitudinal relaxation time* T_1 is the characteristic time of reaching the equilibrium magnetization $\vec{M}_0$ when only $\vec{B}_0$ is applied. The *transverse relaxation time* T_2 is the characteristic time of the decay of $\vec{M}_\perp$ due to the dephasing of the spins [1]. By carefully selecting the timings in the measurement sequences, the NMR signals can be weighted based on T_1 or T_2 to create contrast between the tissues [2].

The NMR signals are usually received by means of Faraday induction. Hence, the measured voltage is proportional to the rate of change of the magnetic flux through the measurement coil, which is proportional to $\Omega_0 M_0 = \gamma B_0 M_0$. Furthermore, the magnetization M_0 scales as B_0, and thus the measured signal is proportional to B_0^2. Because of the quadratic dependence, relatively high measurement fields, i.e., large magnets (> 0.5 T) are favored in MR imaging. Conventional high-field MRI uses large superconducting electromagnets, which are expensive and large in size. In ULF MRI, the requirement of a strong measurement field is relaxed as explained in the following section.

2.1.2 Imaging with ultra-low fields

In ultra-low-field MRI, the measurement fields are typically on the order of 10–100 μT, which corresponds to a Larmor frequency of a few kHz [6, 7, 8]. Imaging with such low fields enables lighter instrumentation and an open geometry for the device. It also improves the capabilities such as imaging in the presence of metals [9], enhanced T_1 contrast [10], and current-density imaging [11]. The amplitude of the measured signal

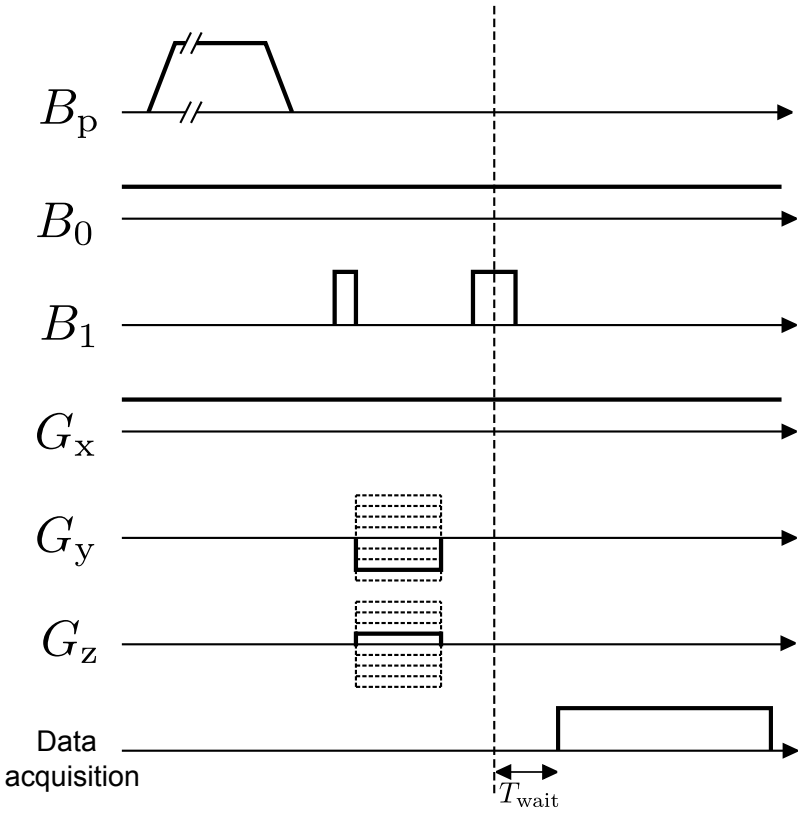

Figure 1: Simplified schematic of the ULF MRI sequence used in Ref. [6]. B_P is the prepolarizing field. B_1 is the oscillating field that flips the magnetization first 90 degrees and then 180 degrees to produce a spin echo (see Ref. [1]). G_y and G_z encode the signal phase. Data are acquired T_wait after the midpoint of the second spin-flip pulse. The frequency-encoding gradient G_x and the B_0 field are kept on constantly.

being so heavily dependent on B_0, Faraday detection becomes very unattractive as B_0 is lowered to the ULF range. To overcome the signal loss, two factors in the imaging process are changed.

First, one replaces the Faraday detection coils with *superconducting quantum interference devices* (SQUIDs) [12]. Instead of measuring the rate of change of the magnetic field, a SQUID responds to the field itself. The absence of frequency dependence in the amplitude of the measured signal makes SQUIDs favorable in low-frequency measurements.

Second, the initial magnetization M_0 is increased by applying a *prepolarizing field* $\vec{B}_\mathrm{p}$ to the sample before the signal acquisition [12], as shown in an example of a ULF MRI pulse sequence in Fig. 1. With prepolarization, the amplitude of the acquired signal becomes completely independent of the measurement field $\vec{B}_0$. Typically, the amplitude of $\vec{B}_\mathrm{p}$ is on the order of 10–100 mT, which yields an approximately 1000-fold increase in the initial magnetization M_0.

The downside in combining prepolarization and SQUID detection is that the strong magnetic pulses given before the signal acquisition disturb the operation of

the sensors. The signal acquisition must be started quickly after the pulses to avoid the signal loss due to the spin relaxation. To restart acquisition, the SQUID feedback must be reset so that it can, again, follow the applied flux signals. Part of the waiting time T_{wait} before starting the data acquisition (see Fig. 1) is caused by transients in the digital SQUID readout after the feedback reset. The reset procedure and the transient effects are discussed more in later sections. In addition, the strong magnetic pulse may trap flux into the superconducting structures, which degrades the SQUID performance. The trapping can, fortunately, be avoided by optimizing the thin-film structures of the device [13].

Another problem relates to the metallic shielding for suppressing external magnetic fields, including the Earth's field. The prepolarizing pulse induces eddy currents in these walls, and the currents generate a secondary field, which can affect the spins and the signal acquisition even long after the pulse [14]. Fortunately, the eddy currents can be reduced by orders of magnitude with a self-shielded polarizing coil [15] or with cancellation waveforms designed to suppress different eddy-current modes in the walls [16]. After applying these techniques, there may, however, still be residual secondary fields, which affect the signal acquisition.

Although brain imaging with ULF MRI has been demonstrated [6, 17], challenges in the quality of the images still remain. The signal-to-noise ratio (SNR) of the acquired images is relatively low due to the weak nature of the spin-induced signals. To approach the quality of high-field imaging, the thermal noise of the system should be suppressed and the sensitivity of the SQUIDs increased. When the SQUIDs are sufficiently tolerant to pulsed fields, the polarizing field B_{p} can also be increased to amplify the NMR signal.

2.1.3 Combination with magnetoencephalography

In *magnetoencephalography* (MEG), the neuronal activity of the brain is studied by measuring the neural-current-generated magnetic fields outside the human head [4]. The simultaneous activation of the neurons on the cortex generates a magnetic field of only 10–1000 fT at the magnetic sensors. The frequency range of these signals is mostly below 1 kHz. Thus, the sensors are required to be extremely sensitive and capable of measuring at low frequencies. To this date, the SQUID has been the most successful device for this purpose [18].

In order to obtain information of the brain activity, the spatial pattern of the magnetic field around the head must be measured with high accuracy. This is why commercial MEG devices contain multiple, typically over a hundred, SQUID sensors in a helmet-shaped configuration. From the principles of electromagnetism, one can derive a model for the measured signals and use it to find a solution for the field source locations.

As both MEG and ULF MRI use SQUID sensors for the magnetic-field detection and work at low magnetic fields, it would be convenient to have the methods in a single device. A hybrid MEG–MRI device can provide both structural and functional information of the brain. Like MEG, also ULF MRI can make use of multiple sensors in an array to increase the SNR and the spatial sensitivity. A magnetically shielded

room protects the field recordings from external disturbances in both methods.

At least two groups have succesfully combined MEG and ULF MRI in a single device. At the Los Alamos National laboratory, Zotev et al. [17] measured ULF MRI and auditory MEG signals with a seven-channel device. At Aalto University, Vesanen et al. [6] converted a commercial 306-channel MEG device into a hybrid MEG–MRI system with a superconducting prepolarizing coil. Without degrading the MEG performance, 48 channels were successfully used to measure structural MRI of a human brain. Nonetheless, in both cases, the SNR of the MR images was below the standard of conventional MRI.

In addition to improved accuracy, one of the main goals in the development of the hybrid system is simplification of the workflow of MEG studies. The neuronal activity solved from the measurements is typically mapped on the structural brain image of the subject. MRI gives detailed information of the structure of the brain, but in order to co-register the MEG data and an MR image, one must know the exact head position and orientation inside the MEG sensor array. The combined MEG–MRI device can reduce the number of possible error sources in this task, since using the same sensors in both methods enables automatic co-registration of the different coordinate systems [19].

2.2 SQUID magnetometers

In this section, I introduce basic principles of the operation of superconducting quantum interference devices. Although a SQUID sensor has its quantum-mechanical nature, understanding the basics of the device does not require all details of the physical theory. A more thorough treatment would involve the phenomenological Ginzburg-Landau theory or the microscopic theory by Bardeen, Cooper, and Schrieffer, which are out of the scope of this thesis.

After getting a qualitative understanding of SQUID operation, I explain the readout, which is based on an integrating feedback element. The third part of this section handles the auxiliary electronics used to couple different signals to the SQUID and to control the SQUID characteristics. In the last part, I discuss the digital implementation of SQUID control.

In this text, I only discuss the DC SQUID, which is the most common type of SQUID used in biomedical measurements. In addition, there is the RF SQUID, which has only one Josephson junction, and the operation of which is slightly more technical [5]. In this work, the term SQUID always refers to the DC SQUID.

2.2.1 Physical principles

The operation of a SQUID is based on physical phenomena in superconducting material. Below the critical temperature T_c, the electrons in the material experience a transition to a lower energy state where they act coherently as pairs (known as Cooper pairs). This coherent behavior of an entire ensemble of superelectrons can be described with a macroscopic wave function [20]

$$\Psi(\vec{r},t) = \sqrt{\rho(\vec{r},t)}\exp\left[i\phi(\vec{r},t)\right], \tag{5}$$

where $\rho(\vec{r},t)$ is the local density of the superelectrons and $\phi(\vec{r},t)$ the phase of the complex wave function. Using the macroscopic wave function and the related Schrödinger-like equation, many superconducting phenomena can be explained.

For a single quantum mechanical particle, one can derive a formula for a probability current using the Schrödinger equation and the conservation of probability (continuity equation) [21]. In the context of the macroscopic wave function, the flow can be *interpreted* as the current density of superelectrons [20, 22],

$$\vec{J} = \mathrm{Re}\left[\Psi^* \frac{1}{m}\left(\frac{\hbar}{i}\nabla - q\vec{A}\right)\Psi\right] = \frac{\hbar}{m}\left(\nabla\phi - \frac{q}{\hbar}\vec{A}\right)\rho\,, \tag{6}$$

where $\frac{1}{m}\left(\frac{\hbar}{i}\nabla - q\vec{A}\right)$ is the velocity operator in the presence of electromagnetic field, m being the effective mass of a superelectron, q the effective charge, and $\vec{A}$ the vector potential related to the electromagnetic field. The second equality is obtained by substituting the macroscopic wave function according to Eq. (5). Looking at this explicit formula, the supercurrent may seem to depend on the gauge of $\vec{A}$, but it turns out [20] that the choice of gauge manifests itself also in the phase of the wave function ϕ, so that Eq. (6) is gauge-invariant.

Consider now a supercurrent flowing in a closed loop. If we integrate Eq. (6) around the loop, the vector potential gives the magnetic flux Φ through the loop. Furthermore, the line integral of $\nabla\phi$ is the phase change around the loop. Besides being zero, it can have a value of any multiple of 2π, which is required for Ψ to be single-valued. Thus, the integrated equation can be written as

$$\frac{m}{\hbar}\oint \vec{J}\cdot d\vec{l} = \oint \nabla\phi\cdot d\vec{l} - \frac{q}{\hbar}\oint \vec{A}\cdot d\vec{l} = 2\pi n - \frac{q}{\hbar}\Phi\,. \tag{7}$$

The supercurrent in the center of the superconductor is typically exponentially small so that we can take a path that forces the term on the left to vanish. Hence, we get

$$\Phi = \frac{2\pi\hbar}{q}n = \Phi_0 n\,, \tag{8}$$

where $\Phi_0 = \dfrac{2\pi\hbar}{q}$ is called as the *magnetic flux quantum*.

The SQUID is a superconducting loop interrupted by two insulating junctions, known as Josephson junctions. A single Josephson junction couples two superconducting electrodes together, so that the supercurrent can tunnel through the junction and create a phase difference δ between the electrodes. Assuming linear coupling between the two superconductors, it can be shown [22, 23] that the supercurrent and voltage across the junction are

$$I_\mathrm{s} = I_\mathrm{c}\sin(\delta) \quad \text{and} \tag{9}$$

$$V = \frac{\Phi_0}{2\pi}\frac{\partial\delta}{\partial t}\,, \tag{10}$$

where I_c is the so-called critical current of the junction. The junction turns partly resistive whenever the driving current through the junction exceeds I_c.

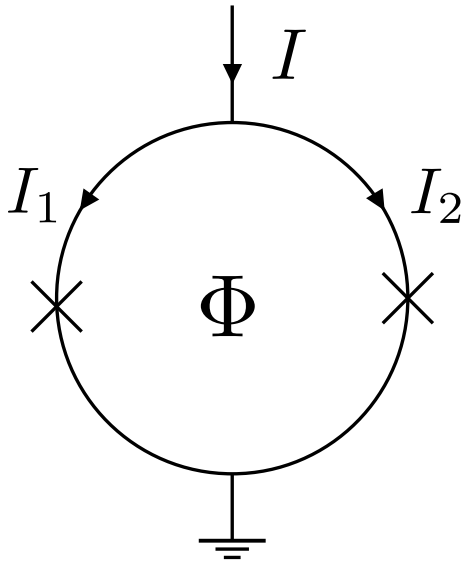

Figure 2: Schematic of a SQUID, grounded from one end, with the two Josephson junctions marked as crosses.

The first Josephson equation, Eq. (9), states that the tunneling supercurrent is sinusoidally dependent on the phase difference of the electrodes. The second one, Eq. (10), gives a relation between the rate of change of the phase and the voltage across the junction. Combining these equations, we can see that, even for a small driving voltage, say 1 μV, across the junction, the current oscillates at about 1 GHz. However, such AC effects are typically not used in low-frequency applications.

Putting two of these junctions in a superconducting ring, as depicted in Fig. 2, leads to interference of the parallel Josephson currents I_1 and I_2 with phase differences δ_1 and δ_2. With a calculation similar to Eq. (7), one can show that the difference between δ_1 and δ_2 is determined by the flux Φ through the loop [20]

$$\delta_2 - \delta_1 = 2\pi \frac{\Phi}{\Phi_0} + 2\pi n \,, \tag{11}$$

where n is an integer. The total current through the two (identical) junctions is then

$$\begin{aligned} I &= I_c \sin(\delta_1) + I_c \sin(\delta_2) \\ &= 2I_c \cos\left(\frac{\delta_2 - \delta_1}{2}\right) \sin\left(\frac{\delta_2 + \delta_1}{2}\right) \\ &= 2I_c \cos\left(\frac{\pi\Phi}{\Phi_0}\right) \sin\left(\delta_1 + \frac{\pi\Phi}{\Phi_0}\right) \,. \end{aligned} \tag{12}$$

Here, $I_{\max} = 2I_c \left|\cos\left(\frac{\pi\Phi}{\Phi_0}\right)\right|$ is the maximum supercurrent that can flow through the two junctions and depends periodically on the flux through the SQUID loop with the period Φ_0.

A real SQUID further has an inductance, and the junctions have capacitances and resistances, which were not yet taken into account. A finite inductance adds a

circulating screening current to the loop, which decreases the modulation depth of $I_{\max}(\Phi)$ [5]. The Josephson junctions may be intentionally shunted with resistors to alter the current-voltage characteristics of the SQUID.

Such additional effects can be described by RCSJ-model (Resistively- and Capacitively-Shunted Junction). RCSJ-model for a single junction can be written as

$$I = C\frac{\partial V}{\partial t} + \frac{V}{R} + I_c \sin\delta\,, \tag{13}$$

where C is the junction capacitance and R the resistance. Substituting the Josephson voltage from Eq. (10) to the equation, one finds nonlinear second-order differential equation for the junction phase difference δ. Modeling both junctions of a SQUID with RCSJ and adding inductive screening current to Eq. (11) leads to two coupled differential equations, which can be solved numerically [5]. Regardless of the parameters put into the equations, the solution for $I_{\max}(\Phi)$ is always periodic with the period Φ_0.

2.2.2 Readout

As described in the previous section, the maximum supercurrent through the SQUID is periodic in the input flux Φ_{in}. When a resistively shunted SQUID is biased with DC current slightly above the critical current of the junctions, a measurable voltage appears [24]. The periodic dependence of the supercurrent can be observed by measuring the average voltage across the SQUID as a function of Φ_{in}. For example, in the limit of low inductance, $L \ll \Phi_0/2I_{\mathrm{c}}$, and low capacitance, $C \ll \Phi_0/(2\pi R^2 I_{\mathrm{c}})$, the measured DC voltage is [20]

$$V(\Phi_{\mathrm{in}}) = R\sqrt{I_{\mathrm{b}}^2 - I_{\max}(\Phi_{\mathrm{in}})^2}, = R\sqrt{I_{\mathrm{b}}^2 - \left[2I_{\mathrm{c}}\cos\left(\frac{\pi\Phi_{\mathrm{in}}}{\Phi_0}\right)\right]^2}\,, \tag{14}$$

where Φ_{in} is the input flux, I_{b} the bias current, $I_{\max}$ the maximum supercurrent through the Josephson junctions, and R the parallel combination of the two resistors shunting the junctions. By varying the SQUID properties like inductance, resistance, parameters of the Josephson junctions, or, most easily, the bias current or voltage, one can affect the shape of the *SQUID transfer function* $V(\Phi_{\mathrm{in}})$.

Alternatively, the SQUID can be biased with a DC voltage and the average current $I(\Phi_{\mathrm{in}})$ can be measured [24]. In the next section, I describe auxiliary electronics of a voltage-bias SQUID. Since the current is turned into voltage by the electronics, I will only use V as a symbol for the SQUID response to avoid any confusion.

The response of the SQUID being highly nonlinear, accurate determination of the input flux requires a dedicated readout scheme. To linearize the response, a feedback flux Φ_{fb} is introduced to the SQUID loop using an external coil. The feedback is usually implemented by integrating the SQUID voltage, multiplying it by an appropriate gain G_{I}, and inductively feeding that signal back to the SQUID with a negative sign, see Fig. 3b. This feedback scheme, commonly known as a *flux-locked loop* (FLL), drives the SQUID voltage towards zero so that the total flux

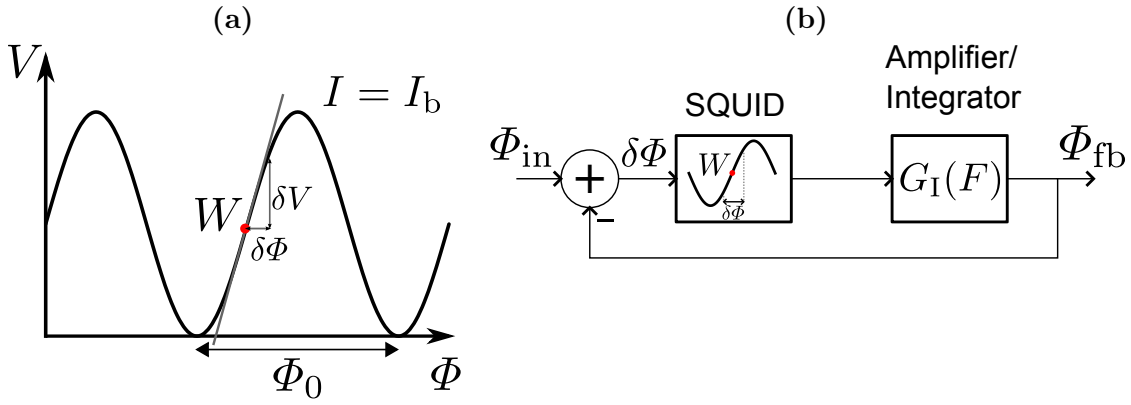

Figure 3: (a) SQUID flux-to-voltage graph and the concept of working point W. (b) Simplified model of a flux-locked loop.

$\Phi_{\mathrm{tot}} = \Phi_{\mathrm{in}} - \Phi_{\mathrm{fb}}$ through the SQUID stays locked to a constant value [5]. As Φ_{tot} does not change, the feedback flux Φ_{fb} follows the input flux Φ_{in}. Consequently, the current in the feedback coil then gives a measure of Φ_{in}.

As the FLL drives the voltage to zero, the zero level of $V(\Phi)$ determines the *working point* W, to which the total flux Φ_{tot} is locked. The zero level of the voltage is adjusted so that the *transfer coefficient*, i.e., slope of the transfer function at W, $V_\Phi = \frac{\partial V}{\partial \Phi_{\mathrm{in}}}\Big|_W$, is maximized. In consequence, the error flux $\delta\Phi$ from W (see Fig. 3a) is transferred to voltage $\delta V = V_\Phi \delta\Phi$ as efficiently as possible. Since the response of the SQUID is periodic, a working point with maximal V_Φ can be found at every multiple of Φ_0.

Assuming the total flux Φ_{tot} is locked to the working point value, the SQUID can be modeled as a linear element with the constant gain V_Φ. If the feedback flux Φ_{fb} is used as an output for the whole system, and Φ_{in} serves as an input, the transfer function of the simplified model is

$$H(F) = \frac{V_\Phi G_{\mathrm{I}}(F)}{1 + V_\Phi G_{\mathrm{I}}(F)}\,, \tag{15}$$

where G_{I} is the integrator gain. The open-loop gain of an integrator diverges at zero frequency, which means that value of the closed-loop transfer function will always be one at sufficiently low frequencies. Since the integrator gain drops towards higher frequencies, the FLL also works as a kind of low-pass filter. Depending on the type of integrator, on delays in the feedback loop, and on other non-idealities in the system, there may be some resonance effects below the roll-off frequency [24].

2.2.3 Electronics

A simplified picture of the electronics for a voltage-biased SQUID is shown in Fig. 4. The SQUID current is preamplified with a transimpedance amplifier, i.e., current signal is turned into voltage. The feedback is implemented digitally, which is the topic of the next section. The working point W is determined by three voltages:

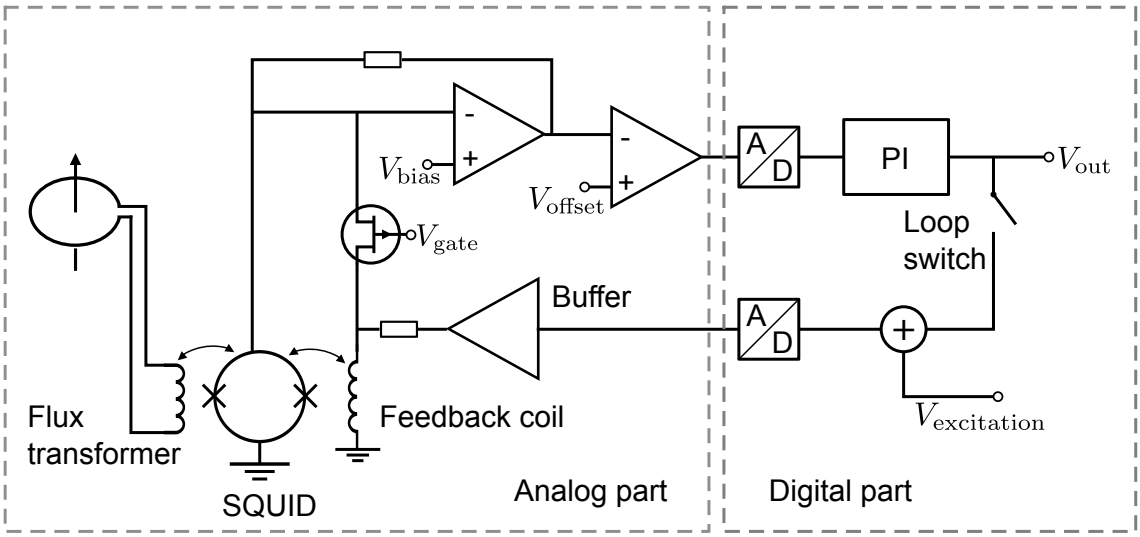

Figure 4: SQUID electronics with simple digital feedback. The figure is modified from Ref. [25].

the bias voltage V_{bias}, offset voltage V_{offset} and gate voltage V_{gate}. The bias voltage controls the modulation depth of the SQUID I–Φ curve, and the offset voltage can be used for setting W to a specific point on the curve.

V_{gate} is the gate voltage of the field-effect transistor, used as a tunable resistor, which controls the positive feedback used in the so called *noise-cancellation* technique [26]. By optimally adjusting the amount of positive feedback with V_{gate}, the noise current from the amplifier can be canceled out. Otherwise, the amplifier noise would contaminate the measurements. The gate voltage also affects the FLL working point so that all the three tuning variables must be optimized together. In Fig. 4, the positive feedback is coupled to the SQUID via the feedback coil.

To avoid degraded performance and possible LC resonance, the SQUID capacitance and inductance are usually designed to be as small as possible. On the downside, a small inductance leads to poor coupling between the external magnetic field and the SQUID loop. This is why the external field signal is coupled to the SQUID most often with a superconducting flux transformer, as illustrated in Fig. 4.

The flux transformer consists of a pickup loop that determines the spatial sensitivity of the device and an input coil that couples the flux signal to the SQUID. Since the flux transformer circuit is superconducting, the total flux through the inductors is fixed [20] and the flux experienced by the SQUID is

$$\Phi_{\mathrm{in}} = \Phi_{\mathrm{p}} \frac{M}{L_{\mathrm{p}} + L_{\mathrm{i}}}, \tag{16}$$

where Φ_{p} is the flux in the pickup coil, M the mutual inductance between the input coil and the SQUID, and $L_{\mathrm{p}} + L_{\mathrm{i}}$ the total inductance of the flux transformer circuit.

Besides measuring the magnitude of the field, a pickup coil can be configured to approximately measure the gradient of the field or even higher-order derivatives. Gradiometers have the advantage that they effectively reject noise signals from

distant sources [5]. On the other hand, their spatial sensitivity limits the capability of imaging sources further away from the pickup coil.

Although a larger number of sensors provides more detailed information of the magnetic field around the imaged object, problems arise when the sensors are brought closer together. The mutual inductances and other interactions between the pickup loops lead to crosstalk, i.e., a single-sensor signal leaks to the neighboring sensors [5]. Besides the magnetic couplings between the pickups, the leaking of the signals can be due to capacitive or inductive interference in the feedback electronics.

One way to reduce crosstalk is to apply the negative feedback, instead of to the SQUID, to the flux-transformer circuit so that the screening current through the pickup coils becomes constant [27]. In practice, the coupling of the feedback can be more complex, especially when an intermediate transformer between the pickup loop and the SQUID is used.

2.2.4 Digital control

Traditionally, the flux-locked loop has been implemented using an analog integrator. In the 1990s, *digital signal processors* (DSPs) had become so advanced that the FLL could be implemented in software [28, 29, 30]. Processing the SQUID signal digitally requires *analog-to-digital* (A/D) conversion between the SQUID and the integrator. This simply means converting the analog voltage into bit representation. After the digital processing, the digital feedback signal is converted to a voltage signal using a *digital-to-analog* (D/A) converter. The converted signal is then applied to the feedback coil through a resistor, as illustrated in Fig. 4.

Digital feedback has advantages in its flexibility, for example, in signal filtering. Changes in the control, which would require a completely different analog implementation, can easily be made in the DSP software. This is especially convenient in multichannel systems, where many SQUIDs can be controlled with the same DSP program.

The advantage of analog electronics, on the other hand, is that it can be substantially faster. With analog electronics, the system bandwidth can be extended beyond the MHz range [24]. Ultimately, the limiting factors can be the signal propagation delay (only 10–100 ns) between the SQUID and the feedback electronics, or the non-idealities in the SQUID preamplifier, e.g., finite bandwidth and noise.

In digital systems, the bandwidth is limited by the DSP sample rate and additional digital delays, for example, in the digital-to-analog conversion. Bracht et al. [29] reported a delay-limited bandwidth of 5 kHz using DSP technology in 1994. The delay in the feedback originated from additional sample delays in serial data handling. Later, in 2001, an ultra-fast digital FLL with only 200 ns of digital delay and a 5-MHz bandwidth was implemented by Ludwig et al. [31], using a complex programmable logic device (CPLD), which has smaller intrinsic delays than a DSP.

An interesting possibility in digital FLLs is to increase the dynamic range of the flux measurements by resetting the FLL every time the flux value exceeds one Φ_0 [28, 32]. The flux quantum jumps are then added to the measured FLL signal to obtain the correct flux data. In order to do this, the digital feedback value corresponding

to Φ_0 should be measured with sufficient accuracy, and the FLL should run fast compared to the measured frequencies.

The bandwidth of a DSP FLL can be extended by introducing an additional proportional signal in parallel with the integrator, as in shown Fig. 4. Consequently, the feedback is a linear combination of the SQUID voltage and its integral. The proportional signal is weighted by a P gain and the integral by an I gain. By optimally tuning these two gains, the response of the closed-loop system can be enhanced. A more quantitative description of the digital PI controller will be given in Sec. 3.2.

In ULF MRI data acquisition, the control of the SQUIDs plays a big role. The field pulses in the sequence exceed the available range of the feedback, which makes the feedback saturate and lose track of the input flux. After the pulses, the operation of the feedback is reactivated by resetting the FLL integrator to zero. The digital integrator is easy to reset, but the early NMR signal is lost because of a transient from the digital system and other undesired effects described in Sec. 3.3. In Sec. 3.4.1, a new digital flux-control algorithm is presented to replace the integrator reset.

2.3 Digital signal processing

An understanding of digital signal processing is needed for analyzing the flux-locked loop. Thus, in this section, I briefly review the basics of the theory of digital signals and systems. For further details, see for example Ref. [33]. Digitally controlled analog systems are usually called sampled data systems. For those, Ref. [34] provides a more theoretical description.

In this work, I use F as a symbol for frequency in natural units, because, in digital signal processing, the lower-case symbol usually denotes the normalized frequency $f = F/F_\mathrm{s}$, where F_s is the signal sampling frequency. The symbol ω denotes the normalized angular frequency $2\pi F/F_\mathrm{s}$, which is a convenient quantity when dealing with discrete-time signals.

2.3.1 Discrete-time signals and systems

Let us denote a discrete-time signal by $x[n]$, where n is an integer. A discrete-time system is a mapping $\mathcal{T}$ of an input signal $x[n]$ to an output $y[n]$. A special and highly applicable class of such systems are *linear time-invariant* (LTI) systems, which follow a general input–output relation [33],

$$y[n] = -\sum_{k=1}^{N} a_k y[n-k] + \sum_{k=0}^{M} b_k x[n-k]\,, \tag{17}$$

where a_k and b_k are constant parameters. Linearity means the output of a linear combination of input signals $\mathcal{T}(ax_1 + bx_2)$ is the same as the linear combination of the individual outputs $a\mathcal{T}x_1 + b\mathcal{T}x_2$. For time-invariant systems, the output of the same input is independent of time shift, i.e., $y[n] = \mathcal{T}x[n]$ if and only if $y[n-k] = \mathcal{T}x[n-k]$ for any time shift k.

LTI systems are conveniently analyzed by the complex Z *transform*. For a *causal signal* $x[n]$, which, by definition, is zero for $n < 0$, the Z transform is defined as

$$X(z) = \sum_{n=0}^{\infty} x[n] z^{-n} \,, \tag{18}$$

where $z \in \mathbb{C}$. The transformed signal is generally denoted by the corresponding capital letter. The Z transform is the discrete equivalent of the Laplace transform, commonly used in electrical engineering and for solving differential equations. It can be proven from the definition that, like the Laplace transform, also the Z transform is linear. Thus, taking a Z transform of Eq. (17) leads to

$$\left(1 + \sum_{k=1}^{N} a_k z^{-k}\right) Y(z) = \sum_{k=0}^{M} b_k z^{-k} X(z) \,, \tag{19}$$

where also the identity $\mathcal{Z}\{x[n-k]\} = X[z]z^{-k}$ has been used.

The *transfer function* $H(z) = Y(z)/X(z)$ characterizes the response of the system. From the previous equation, we get

$$H(z) = \frac{Y(z)}{X(z)} = \frac{\sum_{k=0}^{N} b_k z^{-k}}{1 + \sum_{k=1}^{M} a_k z^{-k}} = G z^{N-M} \frac{\prod_{k=1}^{N}(z - z_k)}{\prod_{k=1}^{N}(z - p_k)} \,, \tag{20}$$

which states that the transfer function of an LTI system is a ratio of polynomials in z^{-1}. The last equality comes from factorizing the polynomials in the numerator and the denominator. Roots of the numerator polynomial z_k are called *zeros* and denominator roots p_k are called *poles*. The zeros, poles and gain G are a compact way to present a transfer function.

2.3.2 Impulse response

Let us introduce the impulse signal $\delta[n]$, which is defined as unity at $n = 0$ and zero elsewhere. The *impulse response* $h[n]$ of a system is simply the output for an impulse $\delta[n]$ as input. Delaying the impulse by k samples, we get $\delta[n-k]$, which only contains a nonzero value at $n = k$. Any discrete-time signal can be written as a series of delayed impulses

$$x[n] = \sum_{k=0}^{\infty} x[k]\delta[n-k] = x[n] * \delta[n] \,, \tag{21}$$

which defines the convolution of $\delta[n]$ and $x[n]$, denoted by $*$.

Using Eq. (21), the output of an LTI system for an input $x[n]$ ($x[n] = 0$, for $n < 0$) can be written as

$$y[n] = \mathcal{T}x[n] = \sum_{k=0}^{\infty} x[k]\mathcal{T}(\delta[n-k]) = \sum_{k=0}^{\infty} x[k]h[n-k] \,, \tag{22}$$

i.e, the output of an LTI system is the convolution of the input $x[n]$ and the impulse response $h[n]$. By taking a Z transform of Eq. (22),

$$\begin{aligned} Y(z) &= \mathcal{Z}\left\{\sum_{k=0}^{\infty} x[k]h[n-k]\right\} = \sum_{k=0}^{\infty} x[k]\mathcal{Z}\{h[n-k]\} \\ &= \sum_{k=0}^{\infty} x[k]H(z)z^{-k} = H(z)\sum_{k=0}^{\infty} x[k]z^{-k} \\ &= H(z)X(z)\,, \end{aligned} \tag{23}$$

we can see that the Z transform of the impulse response $h[n]$ is the transfer function $H(z)$.

LTI systems can be classified into *finite-impulse-response* (FIR) and *infinite-impulse-response* (IIR) systems. An FIR system follows an input–output relation where the output depends only on a finite number of the past input values [$a_k = 0$, $\forall k$ in Eq. (17)]. An IIR system is a recursive system whose output $y[n]$ depends on at least one of the previous outputs $y[n-k]$, and thus the impulse response becomes infinite. In terms of poles and zeros, an FIR system only contains zeros in the transfer function, whereas an IIR system contains at least one pole. Systems with feedback elements can be difficult to solve in the time domain. In Z domain, they can be conveniently analyzed by examining the poles and zeros of the transfer function.

The stability of a discrete-time system can be determined from its impulse response. For a bounded input, the output is also bounded for every time instant if

$$\sum_{n=0}^{\infty} |h[n]| < \infty\,, \tag{24}$$

where the system is assumed to be causal, i.e., $h[n] = 0$ for $n < 0$. It can be shown this condition is equivalent to the situation where all the poles of $H(z)$ lie inside the unit circle on the complex plane [33].

2.3.3 Frequency response

Regarding the FLL, an important concept is the *frequency response* of the system $H(\omega)$: $\mathbb{R} \mapsto \mathbb{C}$. Here, ω is the normalized angular frequency $\omega = 2\pi F/F_\mathrm{s}$, where F_s is the sampling frequency of the digital signal. The relationship between the frequency response and the transfer function is given by

$$H(\omega) = H(z)|_{z=e^{i\omega}} = \sum_{n=0}^{\infty} h[n]e^{-i\omega n}\,, \tag{25}$$

i.e., the frequency response is the Z transform evaluated at the unit circle on the complex plane. From the explicit form on the right, we can see that the frequency response equals the *discrete-time Fourier transform* (DTFT) of the impulse response $h[n]$. The Z transform can thus be interpreted as a generalization of the discrete-time Fourier transform.

The same analysis applies to signals: the frequency content of a signal $x[n]$ can be found by taking Z transform and evaluating it at the unit circle. Rewriting Eq. (23) at the unit circle of the z plane yields

$$Y(\omega) = H(\omega)X(\omega)\,, \tag{26}$$

which states that an LTI system handles the different frequency components of the input signal independently so that each of them are amplified by $|H(\omega)|$ and phase-shifted by $\angle H(\omega)$. Hence, LTI systems can also be thought of as frequency-selective *filters*.

The transfer function diverges at poles p_k; therefore, one can conclude that, if a pole is a near certain frequency ω at the unit circle, that frequency will have a large gain $|H(\omega)|$. On the other hand, if a zero z_k is close to that frequency, that component is attenuated. Hence, examining poles and zeros tells a great deal about the frequency response of the system. As a conclusion to the topic, an example of a simple discrete-time system is depicted in Fig. 5 in different domains.

The frequency response describes the so called *steady-state response* of the system, where the assumption is that the input signal has been applied to the system for an infinite time. In addition to the steady-state response, real-time systems also show a *transient response*, which depends on the signal applied at $n = 0$ and the initial internal state of the system. The transient response distorts the measurement of the steady-state frequency characteristics if the applied signal is not long compared to the memory of the system. This is problematic especially in IIR filters, which have long memories of the past inputs.

2.3.4 Sampling and reconstruction

Ideal uniform sampling transforms a continuous-time (analog) signal $x_\mathrm{a}(t)$ into a discrete-time signal by $x[n] = x_\mathrm{a}(nT)$, where $T = 1/F_\mathrm{s}$ is the sampling interval. This is only a mathematical model, but can be used to analyze a sampled signal. Analyzing the discrete-time Fourier transform of $x[n]$ and the Fourier transform of $x_\mathrm{a}(t)$ leads to the relation [33]

$$X(F) = F_\mathrm{s} \sum_{k=-\infty}^{\infty} X_\mathrm{a}(F - kF_\mathrm{s})\,. \tag{27}$$

Different frequency bands $F \in [kF_\mathrm{s}, (k+1)F_\mathrm{s}]$ fold on top of each other, distorting the original signal, which is graphically illustrated in Fig. 6.

This *aliasing* effect can be avoided by restricting the bandwidth B of the analog signal below the *Nyquist frequency*, $F_\mathrm{s}/2$. Since typical analog signals are not bandlimited, they must be filtered before the sampling. An ideal analog antialiasing low-pass filter would be

$$H_\mathrm{a}(F) = \begin{cases} 1, & |F| < F_\mathrm{s}/2 \\ 0, & \text{otherwise} \end{cases}\,, \tag{28}$$

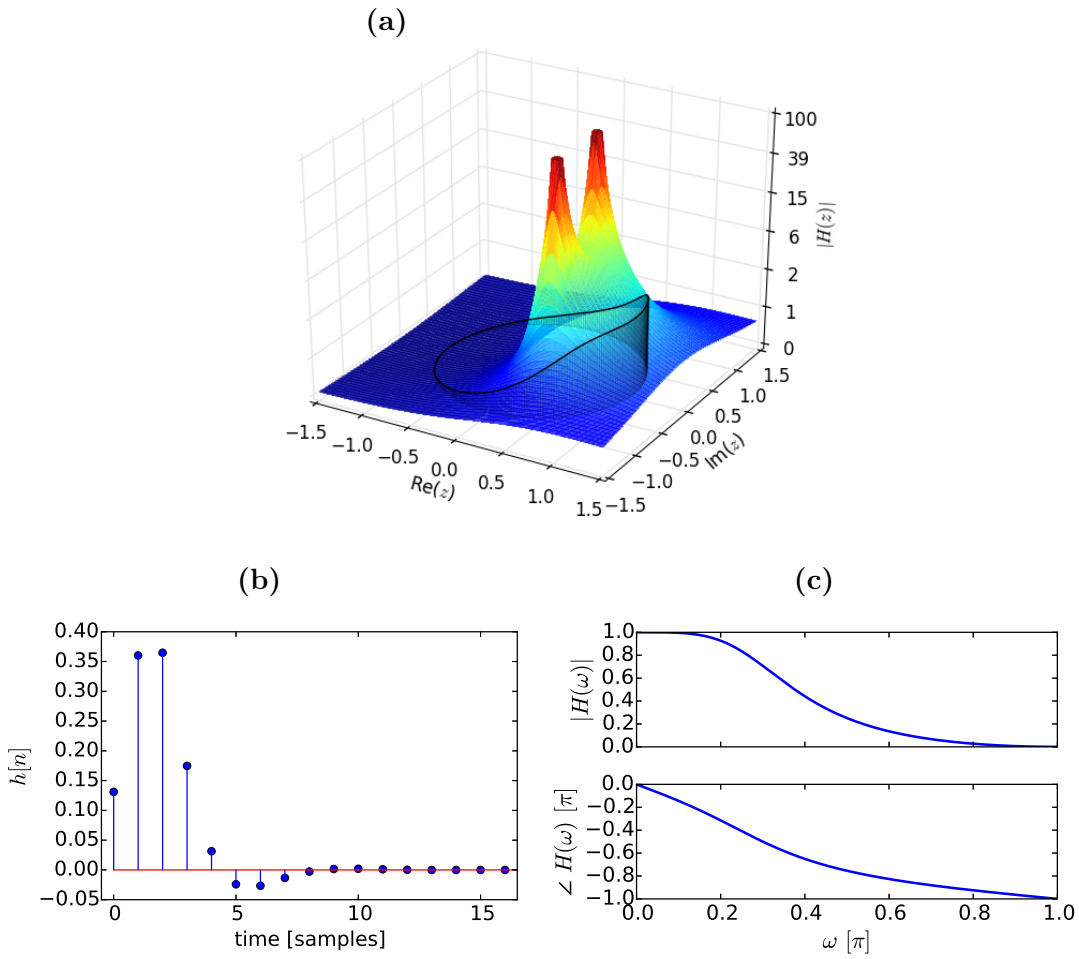

Figure 5: Example of a discrete-time system: a two-pole IIR low-pass filter. (a) Amplitude of the filter transfer function. The frequency response amplitude $|H(\omega)|$ on the unit circle is marked with the solid line. The scale of $|H(z)|$ is linear up to $\max(|H(\omega)|) = 1$ and logarithmic above that to illustrate the poles. (b) Impulse response of the filter. (c) Frequency response of the filter.

which is, however, unrealizable, because of the infinitely sharp roll-off. In real filters, there is a finite transition band where $0 < H_\mathrm{a}(F) < 1$ and, hence, one has to make a trade-off between amplitude distortion below $F_\mathrm{s}/2$ and aliasing due to insufficient attenuation above $F_\mathrm{s}/2$.

Another cause of distortion is signal quantization in the A/D converter (ADC). The ADC maps the analog values into a digital representation, causing some rounding error. Ideally, an ADC works as a linear element and the conversion error is white, which means that the quantization error is distributed over the whole range of the spectrum. In practice, the samples and thus the rounding errors are always at least slightly correlated. However, the effect of signal quantization is small if the applied signals are large compared to the quantization step.

In theory, sampling does not cause information loss for bandlimited ($B \leq F_\mathrm{s}/2$) signals. The discretized signal $x[n] = x_\mathrm{a}(nT)$ can be converted back to the original

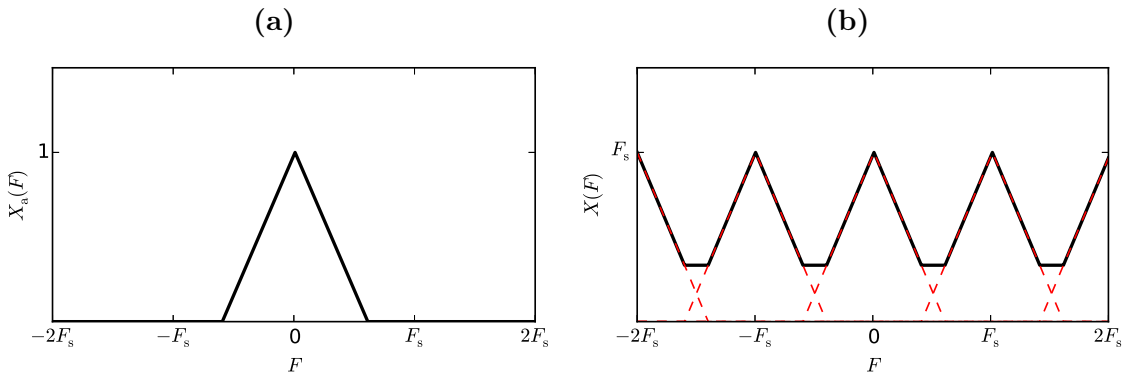

Figure 6: (a) Spectrum of an analog signal $x_a(t)$. (b) Aliased spectrum of the same signal sampled at F_s. The red dashed lines represent the individual aliased bands and the solid line black is the sum of those. The frequencies close to the Nyquist frequency $F_s/2$ are distorted by the interference from the neighboring bands. Although

analog signal $x_a(T)$ by the ideal sinc reconstruction formula [33],

$$x_a(t) = \sum_{n=-\infty}^{\infty} \frac{\sin[\pi(F_s t - n)]}{\pi(F_s t - n)} x[n]\,. \tag{29}$$

Because of its non-causal nature, the formula is inapplicable in real-time signal processing, and hence, digital-to-analog converters (DAC) use simpler techniques such as zero-order hold [34]. Such hold circuits can be interpreted as filters that attenuate higher frequencies in the periodic aliased spectrum. The frequency response is, however, far from the ideal filter, which perfectly attenuates the components above the Nyquist frequency, i.e., the same filter as presented in Eq. (28). To reduce the artificial frequency components above the Nyquist frequency, DACs are usually accompanied with smoothing analog low-pass filters.

Problems with aliasing may arise if the input low-pass filter or the DAC smoothing filter does not sufficiently attenuate the high-frequency components. When using a digital-analog feedback loop, resampling the feedback signal folds the already aliased sideband components $\pm F + kF_s$ back to the lower frequencies, distorting the signal of interest. Such a system can be considered time-invariant only for inputs with such low frequencies that the aliasing does cause a considerable effect [34].

Furthermore, the spectrum aliasing has to be taken into account when down-sampling, or decimating, a discrete-time signal into a new sampling rate $\tilde{F}_s < F_s$. Signals must be low-pass filtered below the new Nyquist frequency $\tilde{F}_s/2$ before the decimation. Otherwise, frequency components between $\tilde{F}_s/2 < F \leq F_s/2$ fold below $\tilde{F}_s/2$, distorting the decimated signal.

3 Materials and methods

In this section, I describe the measurement setup for which the new SQUID control software was written. I introduce a discrete-time model for the digital flux-locked loop, which maintains the SQUID working point during signal acquisition. Finally, I present the methods and algorithms related to the new SQUID control and readout.

3.1 Measurement system

The measurement system (Fig. 7), described in Ref. [6], combines MEG and MRI in the same device. It is based on a commercial multi-channel MEG system by Elekta Oy (Helsinki, Finland). The system includes a helmet-shaped SQUID-sensor array inside a liquid-helium dewar that keeps the sensors superconducting. The MEG measurement system is equipped with MRI coils and a special superconducting prepolarizing coil inside the helium bath. These parts are placed inside a magnetically shielded room, which consists of layers of aluminium and mu-metal to attenuate different frequencies of the external magnetic noise.

The relatively high prepolarizing field pulse can lead to flux trapping in the superconducting material, which deteriorates the SQUID performance. This is why the SQUIDs of the original MEG system were replaced with ULF-MRI-tailored field-tolerant SQUIDs described in Ref. [13]. The SQUIDs were fabricated using thin-film technology and arranged in sensor units, each of which consists of one magnetometer and two orthogonal planar gradiometers (Fig. 7c). The field tolerance was enhanced by adding niobium plates both above and below the center of the thin-film module. The plates were designed to protect the SQUIDs from the direct pulsed field, while not reducing the field sensitivity of the pickup coils too much.

The polarizing field still couples to the SQUIDs via the pickup coils. This issue is mitigated by inserting a *flux dam* [35] in series with the pickup coil. A flux dam is essentially a series of Josephson junctions that switches to normal state when the critical current is exceeded, thus preventing any further build-up of current [3]. Once the field is stabilized, the flux dam should switch back to the superconducting state for signal acquisition.

The SQUIDs are controlled by software (Elekta Oy) that runs on digital signal processors. Each DSP maintains the flux-locked loop of 12 different sensor channels at a 60-kHz sampling rate. The FLL software consists of a digital PI controller, a loop switch, and an excitation signal channel schematically illustrated in Fig. 4. The excitation channel in the software can be used for feeding special control signals to the SQUID via the feedback coil.

The DSPs have a 24-bit architecture and the feedback is calculated in the same precision. The SQUID signal is sampled with only 12 bits of accuracy, which is, however, adequate because the input signals are small in the FLL mode. The input range can be configured to either 1 V or 10 V. The 1-V range yields a better resolution but is saturated by the SQUID transfer function; with the 10-V range, the full modulation of the SQUID can be observed.

The acquired data is low-pass-filtered with a combined FIR–IIR filter and down-

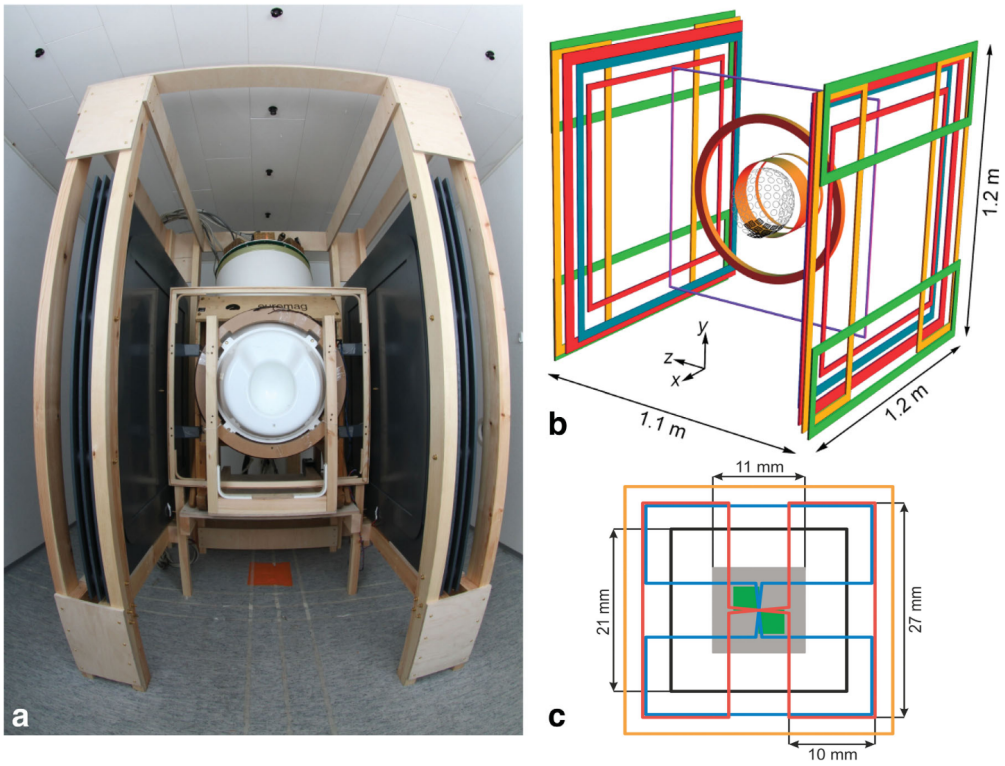

Figure 7: MEG–MRI measurement setup, modified from Ref. [6]. (a) Photograph of the parts of the measurement setup at Aalto University that are inside the magnetically shielded room. (b) Schematic drawing of the coil arrangement and the sensors. (c) Pickup coils of a single sensor unit: black lines represent the magnetometer coil, blue and red lines the gradiometers.

sampled to 10 kHz or below before it is sent to the measurement computer. The FIR filter has its cut-off around 3300 Hz and is used before decimating the signal from 60 kHz to 10 kHz. The IIR filter can be tuned for even lower cut-off frequencies, which enables further down-sampling. By default, the IIR filter is used even if the sampling rate is the maximum 10 kHz. The maximum data acquisition rate restricts the usable bandwidth below the FIR filter cut-off, which also determines an upper limit for B_0 in NMR studies. A larger B_0 field would require real-time demodulation within the DSP program.

3.2 Model for digital feedback loop

In order to study the frequency response of the SQUID in a digital flux-locked loop, a model for the loop response is now presented. Since the data processing is implemented on DSPs, I will model the situation in discrete time. The model assumes that the error flux varies only within the linear range around the FLL working point, which makes the SQUID a linear element. Other analog parts of the

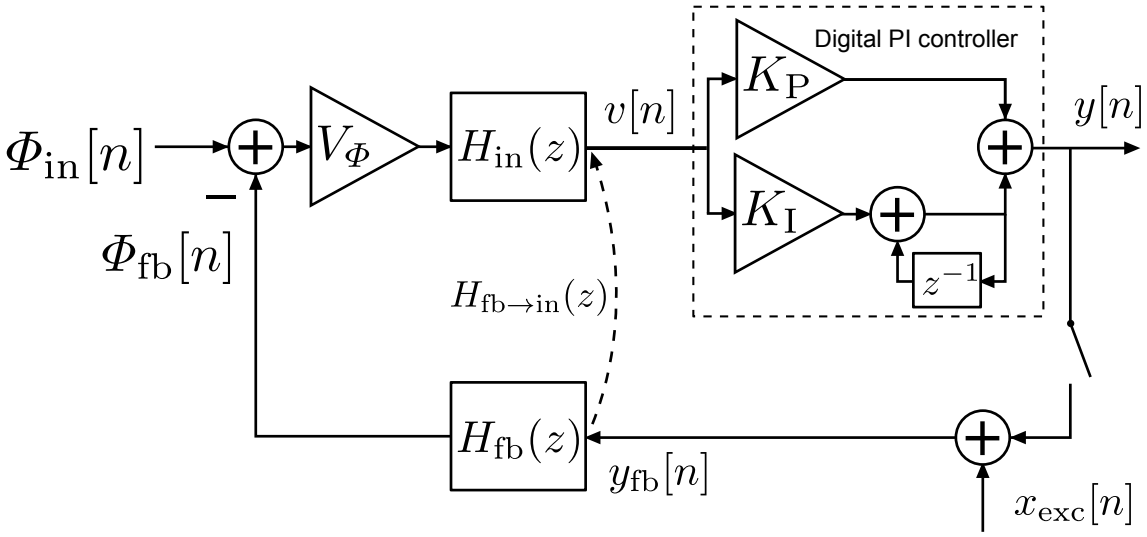

Figure 8: Discrete-time model of the FLL.

system are also assumed to be linear and time-invariant at the sampling instants. For instance, sampling is periodically time-varying operation in continuous time, but synchronized with the computer clock. The signals of interest are assumed to only contain frequencies low enough that possible aliasing effects from sampling do not affect them.

The FLL model is presented schematically in Fig. 8. The signal $\Phi_{\mathrm{in}}[n] = \Phi_{\mathrm{in,a}}(n/F_{\mathrm{s}})$ is the input flux from the flux transformer at the sampling instants, and the output $y[n]$ is the digital reading from the PI controller. The SQUID is modeled as a summing element and the constant gain V_Φ, which is the transfer coefficient at the FLL working point. The digital input has a specific (low-pass) response $H_{\mathrm{in}}(z)$, which depends on the characteristic of the A/D converter and other input electronics. The feedback response $H_{\mathrm{fb}}(z)$ that transforms the digital feedback values $y_{\mathrm{fb}}[n]$ to the feedback flux $\Phi_{\mathrm{fb}}[n] = \Phi_{\mathrm{fb,a}}(n/F_{\mathrm{s}})$ depends essentially on the D/A converter and associated hardware. In this simplified model, H_{in} and H_{fb} are assumed to have unit DC gains, whereas V_Φ includes all the constant analog gains like the preamplifier gain.

Next, let us examine the purely digital, i.e., the software part of the loop. The PI controller consists of a proportional gain K_{P} and an integral gain K_{I} in parallel. The integration is implemented using a simple backward difference approximation of the integral. From Fig. 8, it can be found that the transfer function of the digital PI controller is

$$H_{\mathrm{PI}}(z) = \frac{K_{\mathrm{I}}}{1 - z^{-1}} + K_{\mathrm{P}} = \frac{(K_{\mathrm{I}} + K_{\mathrm{P}}) - K_{\mathrm{P}} z^{-1}}{1 - z^{-1}}\,. \tag{30}$$

Compared to a mere integrator, the parallel proportional gain adds a controllable zero to the transfer function. The DSP implementation contains an additional gain of 256 in series with the PI controller, but in the model, it is included in the gains K_{P} and K_{I}. The digital part also contains a loop switch that is used to toggle the FLL on and off. After the switch, a multipurpose excitation signal $x_{\mathrm{exc}}[n]$ can be

added to the feedback.

Before introducing a closed-loop transfer function for the FLL, I present some remarks of the input and feedback signals. In the discrete-time model, also the input flux $\Phi_{\mathrm{in,a}}(t)$ is modeled at discrete time points. In reality, the sampling happens in the ADC and H_{in} is actually a continuous-time system, which does not have a discrete-time impulse response. In order to get a well-defined transfer function for the FLL, $x[n] = (h_{\mathrm{in,a}} * \Phi_{\mathrm{in,a}})[n]$ will be treated as the input to the system. The notation means a sampled continuous convolution of the functions $h_{\mathrm{in,a}}(t)$ and $\Phi_{\mathrm{in,a}}(t)$. Thus, the signal $x[n]$ is the input flux affected by the input response but not by the SQUID gain V_Φ, i.e., it has units of flux, not voltage. The Z transform of the convolution will be denoted as $X(z) = (H_{\mathrm{in}}\Phi_{\mathrm{in}})(z)$.

Next, consider the response of the PI input $v[n]$ to the digital feedback signal $y_{\mathrm{fb}}[n]$, i.e, the *feedback-to-input response* $H_{\mathrm{fb}\to\mathrm{in}}(z)$. The response is partly analog, but it is shown in Ref. [34] that such a response has a discrete-time transfer function when the DAC and the ADC operate in synchrony. The combined transfer function $H_{\mathrm{fb}\to\mathrm{in}}(z) = (H_{\mathrm{fb}}V_\Phi H_{\mathrm{in}})(z)$ is well-defined, although it is *not* the same as $H_{\mathrm{fb}}(z)V_\Phi H_{\mathrm{in}}(z)$, where $H_{\mathrm{in}}(z)$ and $H_{\mathrm{fb}}(z)$ approximate the continuous-time transfer functions.

With the help of $H_{\mathrm{fb}\to\mathrm{in}}(z)$, we can define the closed-loop FLL transfer function between the input-affected flux $X(z) = (H_{\mathrm{in}}\Phi_{\mathrm{in}})(z)$ and the output $Y(z)$ as

$$H_{\mathrm{FLL}}(z) = \frac{Y(z)}{X(z)} = \frac{V_\Phi H_{\mathrm{PI}}(z)}{1 + H_{\mathrm{fb}\to\mathrm{in}}(z)H_{\mathrm{PI}}(z)}\,, \tag{31}$$

which is determined only by the PI controller response $H_{\mathrm{PI}}(z)$, the SQUID gain V_Φ and feedback-to-input response $H_{\mathrm{fb}\to\mathrm{in}}(z)$. The transfer function $H_{\mathrm{PI}}(z)$ is described in Eq. (30) and depends only on the software gains K_{I} and K_{P}. Furthermore, $H_{\mathrm{fb}\to\mathrm{in}}(z)$ and its DC gain V_Φ can be measured with excitation signals applied to $x_{\mathrm{exc}}[n]$, as explained in Sec. 3.4.2. Hence, the closed-loop transfer function $H_{\mathrm{FLL}}(z)$ can be calculated after determining $H_{\mathrm{fb}\to\mathrm{in}}(z)$.

Although the input response in the time domain, $h_{\mathrm{in,a}}(t)$, is a continuous function and cannot be represented exactly in discrete time, its frequency response $H_{\mathrm{in}}(F)$ up to the Nyquist frequency can be determined. A method for the frequency response measurement is presented in Sec. 3.4.3. If $H_{\mathrm{in}}(F)$ is not uniform at the frequencies of interest, it can create an artifact in the acquired signal. After the response is measured, $H_{\mathrm{in}}(F)$ can be used to further compensate the input flux signal.

3.3 Feedback loop reset

In a ULF MRI imaging sequence, during the field pulses, the input signal is likely to be so large that the feedback saturates and fails to track the input. To reactivate the feedback, the FLL integrators are nulled so that also the feedback flux Φ_{F} becomes zero (apart from the small proportional part). Hence, the total flux through the SQUID corresponds to the input flux, or $\Phi_{\mathrm{tot}} = \Phi_{\mathrm{in}}$, which is practically arbitrary and can correspond to any point on the curve $V(\Phi)$.

After this, it is desired that the SQUIDs can reach their stable working points as quickly and as reliably as possible. The PI controller drives the SQUID voltage to

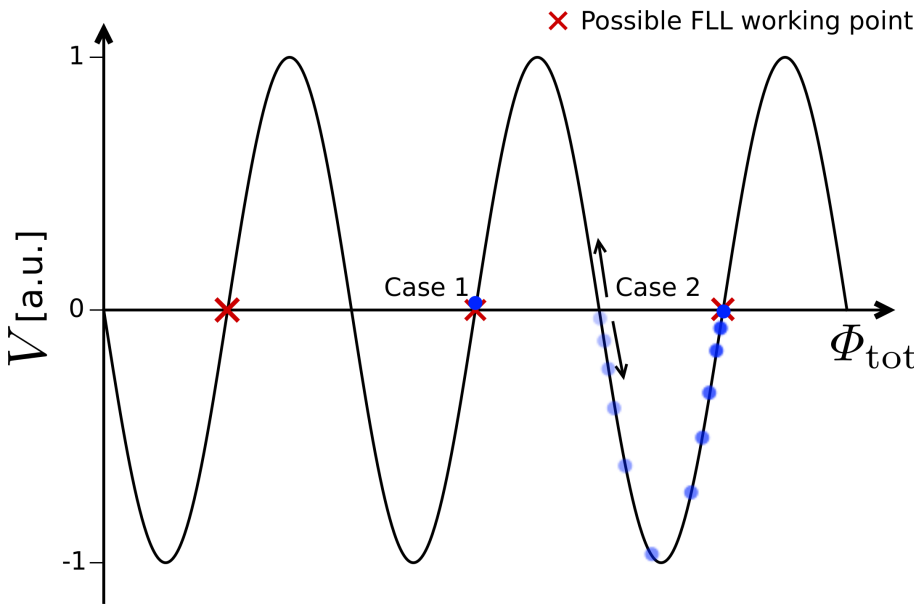

Figure 9: Two cases of the initial flux after feedback loop reset. Case 1: The initial total flux corresponds to an FLL working point. Case 2: The initial total flux corresponds to a point with a negative slope, and the FLL converges to the next working point after being switched on.

zero and locks Φ_{tot} to a constant working point value. The operation of the controller can be seen as analogous to Newton's iteration for finding a root, except that the derivative of the function $V(\Phi)$ is unknown. Since $V(\Phi)$ is very non-linear and the derivative is replaced by a constant gain, it takes many iterations for the feedback to converge. The settling time of the FLL depends on the input flux through the SQUID during the reset and on the gains of the controller.

We can consider two extreme situations. In Case 1, Φ_{tot} happens to correspond to a zero crossing on the positive slope of $V(\Phi)$, see Fig. 9. As the FLL is switched on, no transient will occur, because the SQUID was already at a suitable working point. In Case 2, Φ_{tot} corresponds to a point on the negative slope of $V(\Phi)$. Depending on the measured voltage δV, the PI controller drives the flux either to the next ($\delta V < 0$) or the previous FLL working point ($\delta V > 0$). In Fig. 9, it is illustrated how the flux and the voltage evolve when $\delta V < 0$. The greater the absolute voltage, the more the PI controller adjusts the feedback. Nevertheless, if the total flux is far from an FLL working point, it can take a relatively long time for the feedback to settle.

An example of measured feedback and voltage signals after the integrator reset is plotted in Fig. 10. In this case, the initial flux is far from the FLL working point. It takes roughly 0.5 milliseconds for the PI controller to converge to the new working point. The plateau in the SQUID response around 0.2 ms is due to the limited range of the ADC in 1-V mode.

An additional issue arises from the flux dam in the input circuit, which may not yet be superconducting during the reset. The dam switches to a resistive state when its critical current is exceeded because of the external field. An illustration of this

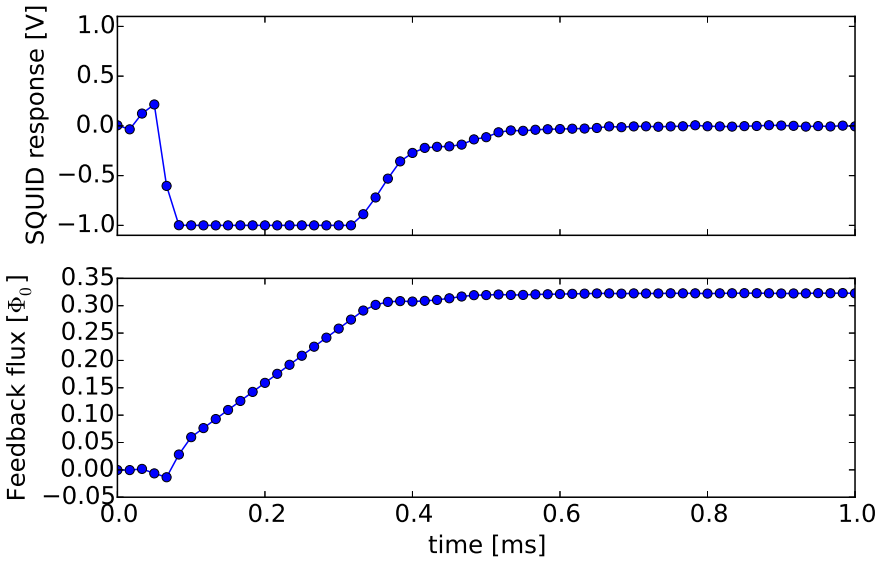

Figure 10: Example of FLL convergence after integrator reset. After 0.5 ms the voltage is roughly zero and the feedback flux has settled.

phenomenon can be seen in Fig. 11, where a high-amplitude triangle wave sweeps the flux using the feedback coil. The periodic response of the SQUID is seen clearly, but when the feedback flux exceeds a certain limit, the modulation disappears. This is when the feedback coupled to the input circuit exceeds the critical current of the flux dam. However, the response is recovered when the rate of change of flux changes its sign.

The same phenomenon can be exploited in the reset; when sweeping the feedback flux back and forth within the critical current of the flux dam, the input circuit is observed to switch back to the superconducting state. This ensures that the SQUID measures the input field in a predicted manner during the following reset phases and the signal acquisition.

In the new reset algorithm, the total flux $\Phi_{\text{tot}} = \Phi_{\text{in}} - \Phi_{\text{fb}}$ is controlled in more detail. First, the nonideal response H_{fb} of the feedback flux Φ_{fb} to the digital feedback signal y_{fb} is taken into account. Because of the delayed low-pass response, it takes a few samples until the flux through the SQUID has settled. Second, the time evolution of Φ_{in} is considered. Decaying eddy currents in the walls of the shielded room generate drift in the input flux Φ_{in}. In order to set Φ_{tot} accurately to the desired value, the rate of change of Φ_{in} during the reset phases has to be measured and compensated. This is discussed more thoroughly in Sec. 3.4.1.

After the FLL, the combined FIR–IIR decimation filter affects the acquired signal by its transient response. When the FLL locks to a new flux value (near zero feedback), the filter experiences a large step signal, generating a transient in the final readout. Because of its sharp cut-off, the filter contains long-lasting ringing in its step response, which corrupts the output signal after the reset. To reduce this transient, the filter states should be reset, as well.

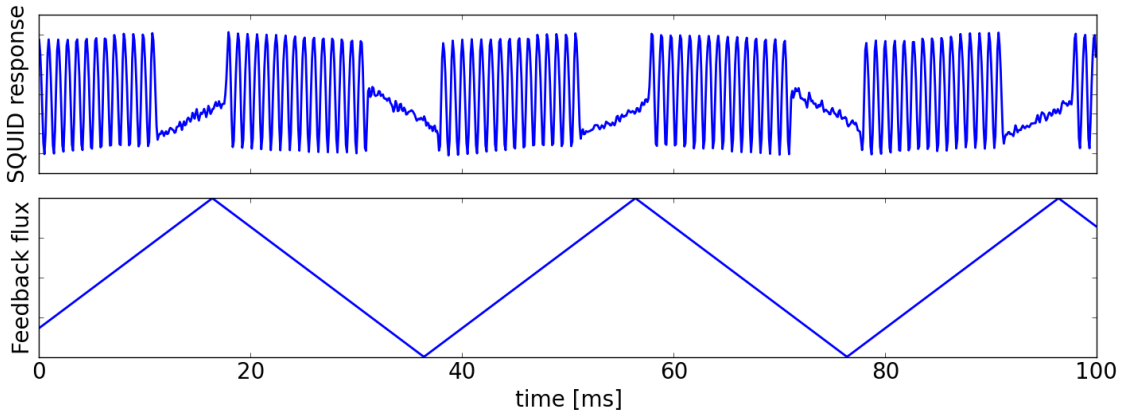

Figure 11: Response of a single SQUID to triangle-wave feedback excitation. The periodic response is recovered every time the sign of the linear sweep is changed.

3.4 SQUID Control software

The new SQUID control functions and measurement procedures were built onto the SQUID controller software by Elekta Oy. The original software contains the digital flux-locked loop with user-specified gains, excitation signal generators, filters, and other supporting functions. The software is mainly implemented in the C programming language and compiled using a special compiler with DSP-specific extensions to the language. The extensions include, for instance, special fractional data types that support fixed-point arithmetic, storage specifiers for efficient use of the DSP memory, and intrinsic functions optimized to use the DSP instructions. In addition, the compiler supports mixing DSP assembly and C.

The main motivation for the new functions was the new FLL reset algorithm for ULF MRI sequences. Also improving the frequency response of the FLL provided motivation for writing functions to measure responses of different parts of the system. Most of the methods were implemented in C and run on the DSPs in real time. Further calculations like discrete Fourier transforms were carried out using Python and the SciPy Stack.

Although the FLL runs at 60 kHz, the final data can only be acquired at 10 kHz or slower. In order to debug and analyze the operation of the new functions, data had to be acquired at 60 kHz at least for the duration of the procedures. For this purpose, multi-purpose data buffers were implemented. The buffers are filled with data in real time during the procedure and read offline after the procedure has been executed. The signals in this work are obtained from those buffers unless mentioned otherwise.

3.4.1 Smart feedback loop reset

A new reset algorithm was designed to address the issues discussed in Sec. 3.3. The key idea is to find a new value for the total flux $\Phi_{\text{tot}} = \Phi_{\text{in}} - \Phi_{\text{fb}}$ that matches an FLL working point as accurately as possible. Then, the total flux Φ_{tot} is driven to a

working point value using the feedback flux Φ_{fb}, while any drift in Φ_{in} is compensated for. Before all these steps, it is ensured that the flux dams are operational by sweeping the feedback flux back and forth. The steps of the new reset algorithm are as follows:

1. Swing the feedback flux back and forth within the critical current range of the flux dam to ensure that the input circuit is in the superconducting state.
2. Find a candidate for the FLL working point by sweeping over one Φ_0 and checking the zero crossings in the SQUID voltage.
3. Calculate the *effective* Φ_0, explained later in this section [Eq. (32)], and compare it to the pre-measured true Φ_0 to estimate the eddy-current-induced drift in Φ_{in}.
4. According to the drift, choose an FLL working point so that the usable feedback range is maximized.
5. Set Φ_{tot} to the working point value by adjusting the feedback. Reset the FLL integrator to correspond to the current feedback.
6. Initialize the decimation filters.
7. Wait for Φ_{fb} to settle, and switch on the FLL.

The feedback signal $y_{\mathrm{fb}}[n]$ and the measured voltage $v[n]$ during the reset are plotted in Fig. 12. The waiting times in the flux swing part are due to the slow response of the feedback. Reset phases 2–3 happen during the linear sweep and 4–6 after the end of the sweep. After that, another 10 samples, i.e., the duration of the step response corresponding to H_{fb} is waited for to ensure that the total flux $\Phi_{\mathrm{tot}} = \Phi_{\mathrm{in}} - \Phi_{\mathrm{fb}}$ has settled to the desired value before switching the FLL (step 7).

In reset phase 2, at least one of the zero crossings within one Φ_0 has a positive slope. The feedback value at this point could be used to set Φ_{tot} to correspond to an FLL working point. However, since Φ_{in} changes during the reset because of external transients, there will be an offset from the working point. If the duration of the reset procedure is small compared to the time scales of the eddy currents, the change in external flux can be assumed linear. Thus, it suffices to estimate the rate of change $\partial\Phi_{\mathrm{in}}/\partial t$ to compensate for the change in Φ_{in} during the time interval between finding the feedback flux Φ_{fb} corresponding to a working point and switching on the FLL.

In phase 3, the rate of change of Φ_{in} is determined by measuring an effective flux quantum $\Phi_{0,\mathrm{eff}}$ from the zero crossings of $V(\Phi_{\mathrm{fb}})$ during the linear flux sweep. A general method for the flux quantum measurement is discussed in Sec. 3.4.4. For this section, we assume that the values of Φ_{fb} at the first and third zero crossings are known. Let these zero crossings correspond to time instants t_0 and t_2. Assuming Φ_{fb} is increasing, and hence Φ_{tot} is decreasing, we can write

$$\begin{aligned}\Phi_0 &= \Phi_{\mathrm{tot}}(t_0) - \Phi_{\mathrm{tot}}(t_2) = [\Phi_{\mathrm{in}}(t_0) - \Phi_{\mathrm{fb}}(t_0)] - [\Phi_{\mathrm{in}}(t_2) - \Phi_{\mathrm{fb}}(t_2)] \\ &= [\Phi_{\mathrm{fb}}(t_2) - \Phi_{\mathrm{fb}}(t_0)] - [\Phi_{\mathrm{in}}(t_2) - \Phi_{\mathrm{in}}(t_0)] \\ &= \Phi_{0,\mathrm{eff}} - \frac{\partial\Phi_{\mathrm{in}}}{\partial t}\Delta t\,, \end{aligned} \tag{32}$$

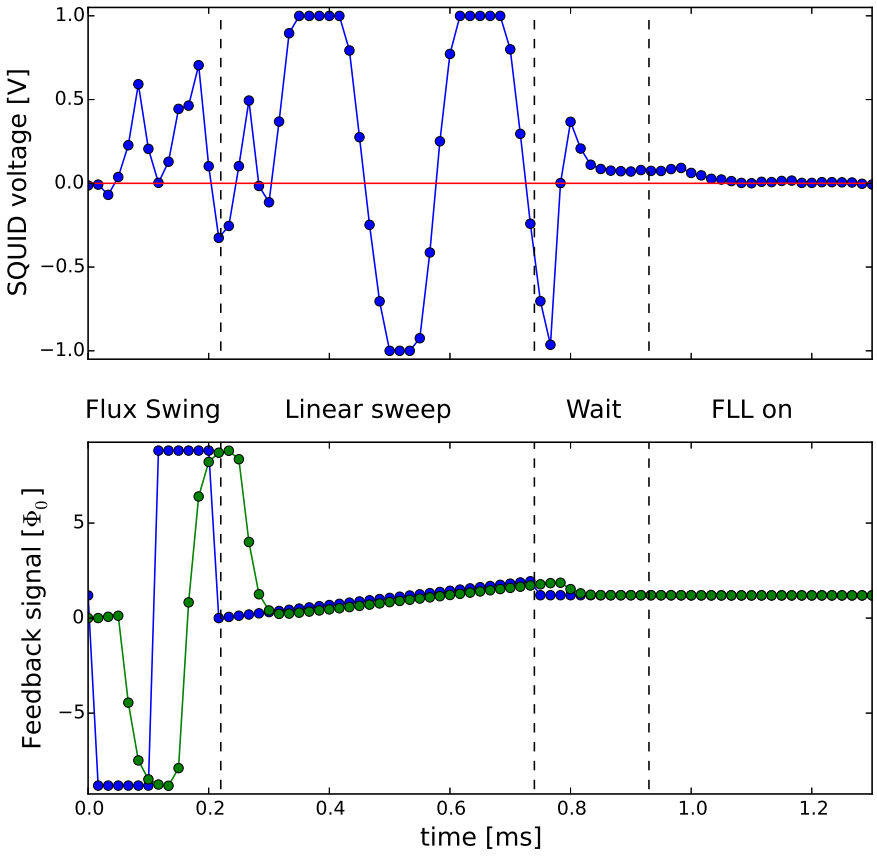

Figure 12: The SQUID input voltage signal $v[n]$ (top) and feedback signal $y_{\mathrm{fb}}[n]$ (blue curve, bottom) during the reset. The green feedback signal is $y_{\mathrm{fb}}[n]$ convolved with the estimated impulse response $\hat{h}_{\mathrm{fb}\to\mathrm{in}}[n]$. During the linear sweep, the SQUID voltage modulation is apparent and the zero crossings can be estimated from the voltage crossing the red line.

where $\Delta t = t_2 - t_0$ and the effective flux quantum is defined as $\Phi_{0,\mathrm{eff}} = \Phi_{\mathrm{fb}}(t_2) - \Phi_{\mathrm{fb}}(t_1)$. Since the true Φ_0 has been estimated earlier, the rate of change of Φ_{in} can be calculated as

$$\frac{\partial \Phi_{\mathrm{in}}}{\partial t} \approx \frac{\hat{\Phi}_{0,\mathrm{eff}} - \hat{\Phi}_0}{\Delta t} \,. \tag{33}$$

We now have the feedback flux for the FLL working point and can compensate for the change of the input flux during the time between finding a working point and switching on the FLL. However, since we have an estimate for the true Φ_0, the feedback flux can be shifted to any possible working point within the range of the DAC. If the flux drift is likely to exceed the DAC range, the feedback flux is set opposite to the drift in reset phase 4. For example, if $\frac{\partial \Phi_{\mathrm{in}}}{\partial t} > \frac{R}{T_{\mathrm{ec}}} > 0$, where R is the DAC range and T_{ec} the eddy current time scale, the feedback is set to the negative end of its range. In consequence, the feedback can follow the input flux twice as long before saturation, compared to if it was initially set close to zero.

Since the smart reset algorithm sets the FLL integrator close to the new working point value, the DC offset in feedback compared to the FLL steady state is small. The decimation filters still have a memory of the old feedback flux value, so their states have to be reset to appropriate values in order to attenuate their transient response. The filter reset is discussed in Appendix B. When the filter states are reset, the transient from the DC offset becomes much smaller and a clean signal can be acquired sooner.

3.4.2 Feedback-to-input response

In order to quantify the FLL closed-loop response H_{FLL}, it is vital to know the feedback-to-input response $H_{\mathrm{fb}\to\mathrm{in}}(z)$ introduced in Sec. 3.2. The response is determined by sampling $H_{\mathrm{fb}\to\mathrm{in}}(\omega)$ at uniformly spaced frequencies using pure sinusoids. As discussed in Sec. 2.3.3, the output of an LTI system for sinusoidal input is the same sinusoid affected by the gain $G = |H(\omega)|$ and the phase shift $\phi = \angle H(\omega)$. The gain and phase shift are measured using quadrature detection.

Before each measurement, the gains $K_{\mathrm{I}} = 0$ and $K_{\mathrm{P}} = 0$ are set to zero, which freezes the FLL integrator in its current state. The sinusoids are applied to the excitation channel $x_{\mathrm{exc}}[n]$, shown in the feedback loop model in Fig. 8, and the loop switch is kept closed. Since the integrator is not updated, the signal $y_{\mathrm{fb}}[n]$ applied to the DAC is the sum of the frozen PI output $y[n]$ and the oscillating excitation signal $x_{\mathrm{exc}}[n]$. Thus, the total flux through the SQUID is

$$\Phi_{\mathrm{tot}} = \Phi_{\mathrm{in}} - (\Phi_{\mathrm{frozen}} + \Phi_{\mathrm{exc}})\,, \tag{34}$$

where Φ_{frozen} is the feedback flux at the FLL working point at the time of freezing, Φ_{exc} the flux from the excitation signal, and Φ_{in} the input flux, which is essentially noise in this context. The amplitude of the excitation signals is set sufficiently small, within the linear range around the FLL working point. The linear range is estimated by assuming the transfer function $V(\Phi)$ to be a perfect sinusoid with a wavelength of Φ_0. Since the excitation amplitude is small, the SQUID transforms the oscillating flux linearly to voltage with the gain V_Φ as illustrated in Fig. 13. The measurement period is kept so short that the noise in the input flux Φ_{in} does have time to drive the total flux Φ_{tot} away from the linear range.

Let the excitation signal be $x_{\mathrm{exc}}[n] = \sin(\omega_{\mathrm{exc}} n)$ with $\omega_{\mathrm{exc}} = 2\pi F_{\mathrm{exc}}/F_s$; the quadrature signal $\cos(\omega_{\mathrm{exc}} n)$ can be generated by phase shifting the sine by the angle $\pi/2$. The system output, here the input to the PI controller, can be written as $v[n] = G\sin(\omega_{\mathrm{exc}} n + \phi) + w[n]$, where $w[n]$ is noise originating from Φ_{in}. Multiplying the output, separately, by the excitation signal and by the quadrature signal gives

$$v[n]\sin(\omega_{\mathrm{exc}} n) = \frac{G}{2}[\cos(\Phi) - \cos(2\omega_{\mathrm{exc}} n + \Phi)] + w[n]\sin(\omega_{\mathrm{exc}} n) \tag{35}$$

and

$$v[n]\cos(\omega_{\mathrm{exc}} n) = \frac{G}{2}[\sin(\Phi) + \sin(2\omega_{\mathrm{exc}} n + \Phi)] + w[n]\cos(\omega_{\mathrm{exc}} n)\,, \tag{36}$$

where standard trigonometric identities have been used. Averaging these products over M full periods of $\sin(\omega_{\mathrm{exc}} n)$ makes the oscillating terms vanish, leaving only the

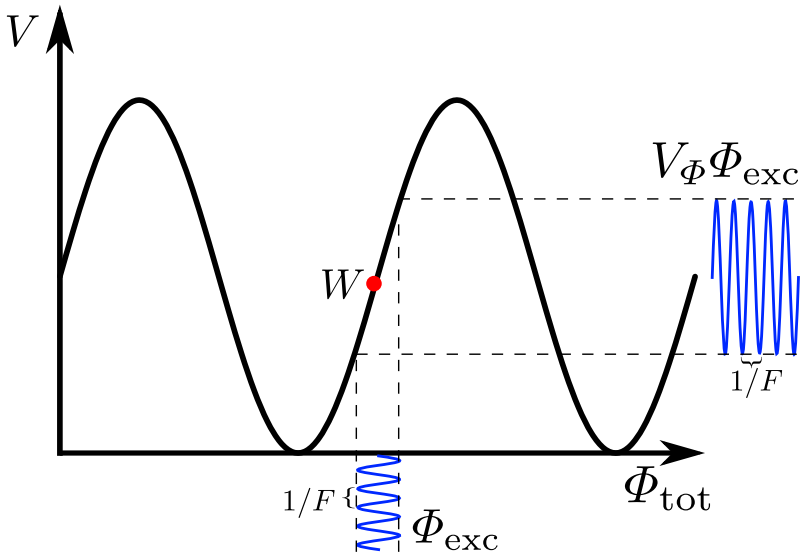

Figure 13: Excitation flux in the feedback response measurement. The excitation flux Φ_{exc} (blue curve on the bottom) varies sinusoidally within the linear range around the FLL working point W. In consequence, the SQUID transfers the signal linearly to $V_\Phi \Phi_{\text{exc}}$ (blue curve on the right).

constant term and the noise term. Assuming that the noise also averages out to a sufficient degree, we get

$$I_1 = \frac{2}{N} \sum_{n=1}^{N} v[n] \sin(\omega_{\text{exc}} n) \approx G \cos(\Phi) \tag{37}$$

and

$$I_2 = \frac{2}{N} \sum_{n=1}^{N} v[n] \cos(\omega_{\text{exc}} n) \approx G \sin(\Phi)\,. \tag{38}$$

The gain can be calculated as $G = \sqrt{I_1^2 + I_2^2}$ and the phase shift as $\phi = \texttt{atan2}(I_2, I_1)$. This is very similar to calculating the coefficients of Fourier series or discrete Fourier transforms (DFT).

The quadrature detection and averaging can also be analyzed in the frequency domain. Multiplying the voltage signal, $G \sin(\omega_{\text{exc}} n + \phi) = \frac{G}{2i}[e^{i(\omega_{\text{exc}} n + \phi)} - e^{-i(\omega_{\text{exc}} n + \phi)}]$, by the quadrature sinusoids can be interpreted as multiplying the a signal by a complex sinusoid $e^{-i\omega_{\text{exc}} n}$, which corresponds to a shift of $-\omega_{\text{exc}}$ on the frequency axis. The analyzed frequency ω_{exc} maps to zero, and the negative-frequency component of the sinusoid to $-2\omega_{\text{exc}}$ as in Eqs. (35) and (36). The averaging can be analyzed using Parseval's theorem

$$\sum_{-\infty}^{\infty} s[n] w^*[n] = \frac{1}{2\pi} \int_{-\pi}^{\pi} S(\omega) W^*(\omega) d\omega\,, \tag{39}$$

where $s[n]$ is now the frequency-shifted voltage and $w[n] = 2/N$ for $0 \leq n < N$ and otherwise zero, i.e, a boxcar signal. The Fourier transform of $w[n]$ is a discrete-time

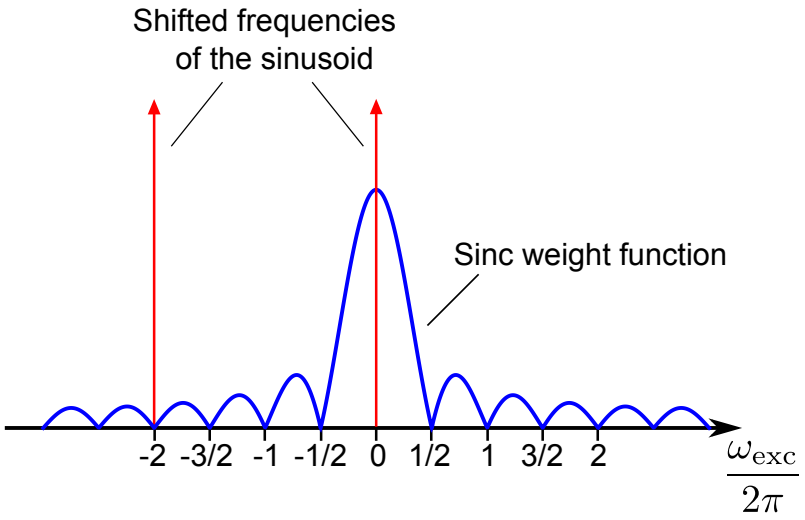

Figure 14: Absolute values of the sinusoid shifted by $-\omega_{\text{exc}}$ and the sinc function in Eq. (40). In this case, the number of cycles in the measurement window (N samples) is $M = 2$. If N does not match full cycles of the sinusoid, the weight of the negative frequency will be nonzero.

sinc signal

$$W(\omega) = \frac{2}{N}\frac{\sin(\omega N/2)}{\sin(\omega/2)} e^{-i\omega(N-1)/2}\,. \tag{40}$$

The zeros of the sinc function match non-zero integer multiples of ω_{exc} when N is chosen to contain M full cycles of the excitation wave, as illustrated in Fig. 14. In consequence, the negative frequency component of the shifted sinusoid at -2ω is damped.

As N is increased, the main lobe of the sinc function narrows down, increasing the resolution in the frequency domain. The interference from the other frequency components in the signals can be analysed using the weight function $W^*(\omega)$. In the actual measurements, the number of acquired samples was $N = 6000$, which corresponds to frequency resolution of 10 Hz (main lobe width) and creates a zero crossing in $W^*(\omega)$ at every 5 Hz.

At the Nyquist frequency $\omega_{\text{exc}} = \pi$, accurate measurement of the signal is difficult, because the sideband component at $2\pi - \omega_{\text{exc}}$ overlaps with the component of interest. In consequence, the gain and phase of the output signal become dependent on the phase of the input signal. Thus, measuring at the Nyquist frequency was avoided.

Finally, let us discuss how the measured frequency response is converted to a time-domain response. By uniformly sampling the upper half of the unit circle, one can get enough data to calculate the impulse response $h_{\text{fb}\to\text{in}}[n]$. The impulse response is real-valued and, hence, the missing data points at negative frequencies can be filled using the conjugate symmetry of the frequency response. The gain at the Nyquist frequency is approximated using a four-point quadratic fit. The DC response of the system is approximated using a very low-frequency signal, but avoiding the line frequency (50 Hz). After getting the full frequency data, the inverse DFT is used for calculating $h_{\text{fb}\to\text{in}}[n]$. It is assumed that the coefficients of $h_{\text{fb}\to\text{in}}[n]$ fall to

zero quickly so that the significant terms in the impulse response can be recovered with the finite number of sampled of frequencies.

3.4.3 Input frequency response

In order to measure NMR signals at higher frequencies, it must be determined how H_{in} affects the acquired signals. The input response could be measured using an external signal generator to apply a field to the pickup. A setup with sufficiently low noise was, however, not easily available at the time of the measurements. Instead, another method was invented for estimating the input frequency response.

The method exploits an excitation signal applied to the feedback and the characteristic periodic response of the SQUID. For the duration of the measurement, the loop switch is opened and a series of linear sweeps, i.e., a triangle wave, is applied to the excitation channel x_{exc}. The feedback system H_{fb} converts this signal to a flux $\Phi_{\text{fb}} = \Phi_{\text{exc}}$ through the SQUID with a systematic delay. During a single linear sweep, the output of the SQUID is almost a sinusoid with the frequency

$$F = \frac{\Delta\Phi}{\Phi_0} F_s \,, \tag{41}$$

where $\Delta\Phi$ is the change in the feedback over one sampling period. An illustration of the signals before and after the SQUID is shown in Fig. 15. The input experiences this pseudo-sinusoid and responds with $H_{\text{in}}(F)$. Using different sweep rates $\Delta\Phi F_{\text{s}}$, the frequency information of the response can be gathered. To observe the full SQUID transfer function modulation for all frequencies, the 10-V input mode is used in this experiment.

Most of the energy of the SQUID output signal is concentrated at the base frequency F, but some of it is in the harmonics. Since the waveform of the SQUID response is always the same, the distribution of the energy in different harmonics should not depend on the sweep rate of the excitation signal. The peak height at the base frequency F can be measured using the quadrature detection with frequency-matched sinusoids from the software signal generator described in Sec. 3.4.2. The noise from the input flux Φ_{in} can suppressed by averaging over many sweeps.

The method works best when the SQUID transfer function is close to a perfect sinusoid. If this is not the case, residual aliasing of the harmonics may generate bias in the measurement at higher frequencies. The finite measurement time limits the frequency-domain resolution. Hence, a total time of 100 ms was used in the measurements. However, when using higher frequencies, the measurements are divided into smaller segments, as the duration of the individual sweeps is shorter. The effective time windows are then smaller, but the number of averaged responses is larger.

The drawback in the method is that the phase information cannot be calculated from the measurements. The feedback response H_{fb} generates a lag in the linear sweep signal, and the SQUID further turns this lag into a phase shift. Also, the noise from the input flux Φ_{in} affects the pseudo-sine phase. Thus, it is difficult to say which part of the output phase originates from the phase response of H_{in}.

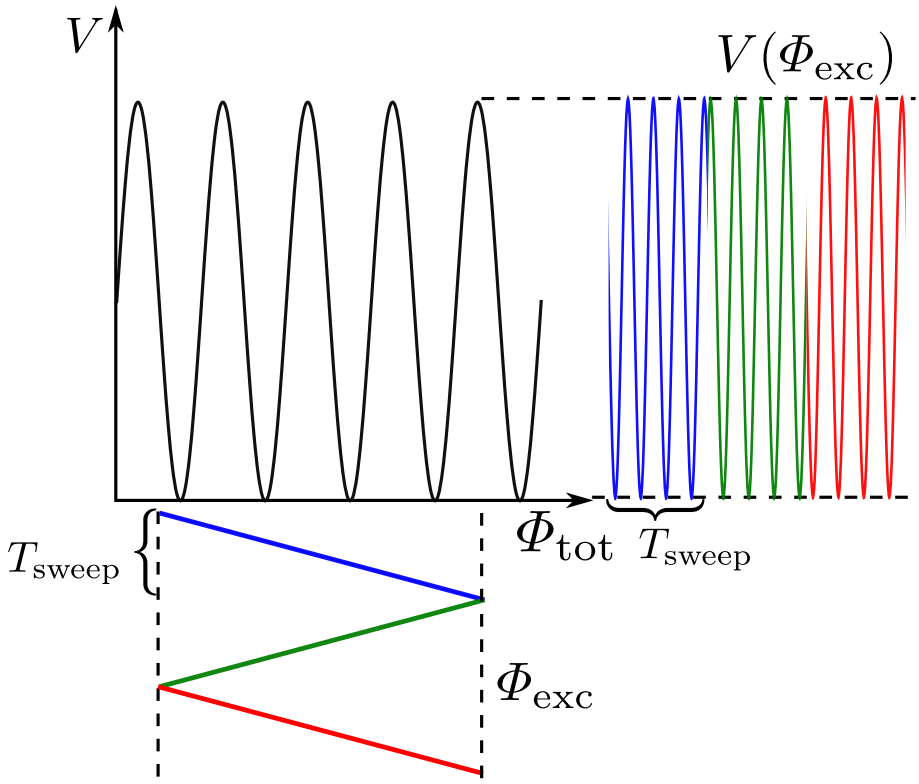

Figure 15: Schematic illustration of the excitation flux Φ_{exc} in the input frequency response and flux quantum measurements. Different colors in Φ_{exc} on the bottom corresponds to the colors in the SQUID output $V(\Phi_{\mathrm{exc}})$ on the right. In practice, there were typically 15–20 wavelengths, i.e., flux quanta, within the sweep range.

3.4.4 Measurement of the flux quantum

The smart reset and frequency response measurements require an estimate for the period of the SQUID response Φ_0. This, of course, corresponds to the known physical constant in SI-units, but what we measure here is the value of Φ_0 *in feedback units*, which depends on the coupling of the feedback to the SQUID. In other words, we determine how much the digital feedback value y_{fb} must be changed in order to change the flux through the SQUID by one flux quantum.

The measurement is based on linearly sweeping the feedback flux through the SQUID as in Fig. 15 and calculating the zero crossings in the SQUID voltage. It is assummed that $\Phi_{\mathrm{tot}} \approx -\Phi_{\mathrm{fb}}$, i.e., the input flux Φ_{in} does not greatly affect the measurement. The flux sweeps are generated by applying a triangle wave to the excitation channel x_{exc}, as in the input response measurements described in Sec 3.4.3. The amplitude of the excitation wave is chosen to be either the full range of the digital feedback or a lower value if the flux dams affect the response described in Sec. 3.3. The feedback response delays the triangle wave and smooths its corners as illustrated in Fig. 16. In consequence, after the turning point, one has to wait a few samples for the sweep rate to settle before the measurement can start. After this, Φ_{fb} changes at the same rate as the digital feedback signal y_{fb}.

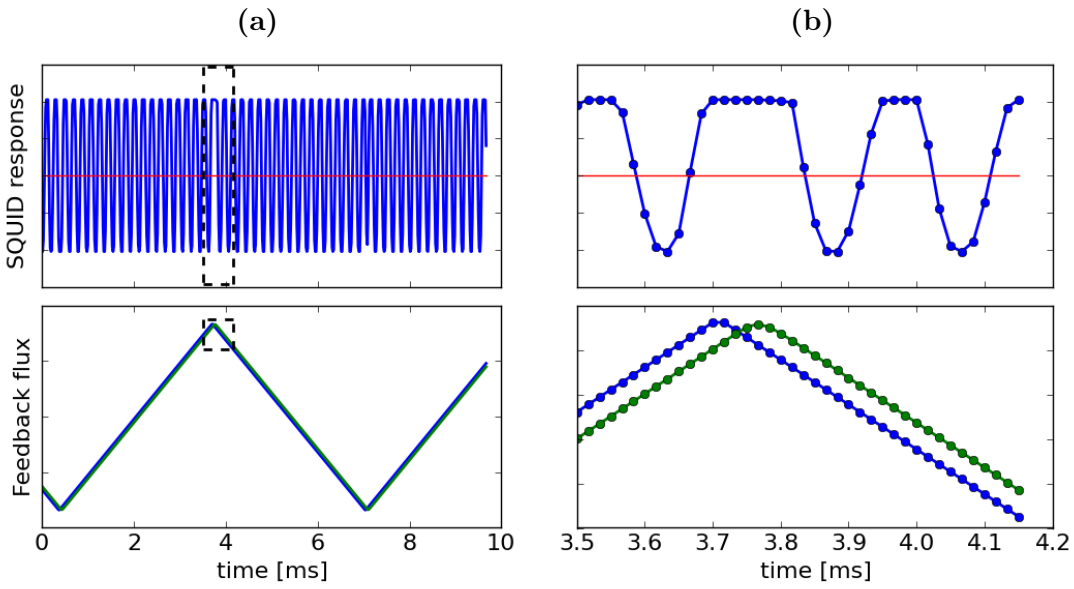

Figure 16: Flux quantum measurement. (a) SQUID response to triangle wave excitation. The red line represents the zero voltage. (b) Close-ups of the dashed boxes in Fig. (a). The wave amplitude saturation originates from the limited range of the ADC. The blue plot in feedback flux is the excitation waveform. The green plot is the estimated delayed waveform seen by the input, calculated using an estimated feedback response $\hat{h}_{\mathrm{fb}\to\mathrm{in}}[n]$. Although this not exactly the same signal as the one in the SQUID, it gives some hint of the feedback delay.

The measurement algorithm detects zero crossings in the signal $v[n]$ by comparing the signs of the previous and current voltage values. The exact flux values at the zero crossings $\Phi_{\mathrm{fb}}(V = 0)$ are linearly estimated using the digital feedback signal $y_{\mathrm{fb}}[n]$ and the voltage $v[n]$ from the time points before and after the crossing. There is, of course, an offset in $y_{\mathrm{fb}}[n]$ compared to the flux $\Phi_{\mathrm{fb}}[n]$, but it cancels out in the final calculation.

After the first zero crossing, every crossing with a slope of the same sign as the first one counts as one Φ_0. The flux quantum count is increased until the next turning point in the excitation wave is reached. In the end of the sweep, an estimate for Φ_0 can be calculated as

$$\hat{\Phi}_0 = \frac{\hat{y}_{\mathrm{fb},p} - \hat{y}_{\mathrm{fb},0}}{p}\,, \tag{42}$$

where p is the number of full flux quanta in the sweep range, $\hat{y}_{\mathrm{fb},0}$ is the linearly interpolated feedback signal at the first zero crossing, and $\hat{y}_{\mathrm{fb},p}$ the interpolated value at the zero crossing after p full Φ_0. Since the feedback sweep is linear, the delay between $y_{\mathrm{fb}}[n]$ and $\Phi_{\mathrm{fb}}[n]$ is constant and thus $\hat{y}_{\mathrm{fb},p} - \hat{y}_{\mathrm{fb},0} \approx \Phi_{\mathrm{fb},p} - \Phi_{\mathrm{fb},0} = p\Phi_0$, which is the rationale for the flux quantum estimate. After reaching the turning point, the procedure is repeated.

Since the measured voltage contains noise, and Φ_{in} can, in practice, affect the

total flux through the SQUID, the linear estimates for the feedback flux are never perfect, even if the adjacent points lie within the linear range around the zero crossing. The noise in $\hat{\Phi}_0$ is, however, reduced when averaging over many sweeps. Should there be a trend in the external flux noise in Φ_{in}, its effect is suppressed when averaging over opposite sweeps.

One still has to consider how to choose the sweep rate of the feedback flux. If the rate is too slow, the external low-frequency flux noise has more time to interfere with the measurement. On the other hand, with a sweep rate that is too fast, the two measurement points around a zero crossing may not lie within the linear range, which causes inaccuracy in flux estimates. During the measurements, it was found that adjusting the rate to correspond to 10–20 samples within one Φ_0 was adequate.

3.4.5 Enhanced digital feedback loop

The main cause of the degraded frequency response of the FLL was found to be a delay in the digital feedback (see Sec. 4.1). The data from the measurements described in Sec. 3.4.2 can be used to calculate an estimate for the impulse response $h_{\text{fb}\to\text{in}}[n]$, which is now used to enhance the frequency response of the whole system. By convolving the digital feedback signal $y_{\text{fb}}[n]$ with the impulse response $h_{\text{fb}\to\text{in}}[n]$, it can be calculated how the feedback is seen by the PI controller. Based on the discussion in Sec. 3.2, the input voltage can be modeled as

$$v[n] = V_\Phi x[n] - h_{\text{fb}\to\text{in}}[n] * y_{\text{fb}}[n]\,, \tag{43}$$

where $x[n] = (h_{\text{in}} * \Phi_{\text{in}})[n]$ is the sampled continuous-time convolution of the input response h_{in} and the input flux Φ_{in}.

From Eq. (43), we can see that the voltage is affected by the non-ideal response $h_{\text{fb}\to\text{in}}[n]$. Ideally, the feedback has only a unit delay, so that the values passed to the DAC at time step n are seen in the PI input at time step $n+1$. The transfer function for this feedback is

$$H_{\text{ideal}}(z) = V_\Phi z^{-1}. \tag{44}$$

To mimic the ideal feedback, we can construct a digital compensation feedback straight to the PI input as in Fig. 17. The idea is to subtract the voltage generated by the estimated $H_{\text{fb}\to\text{in}}(z)$ and add the voltage generated by an $H_{\text{ideal}}(z)$. Using estimates $\hat{V}_\Phi$ and $\hat{H}_{\text{fb}\to\text{in}}(z)$, the transfer function of the compensation feedback can be written as

$$H_{\text{comp}} = \hat{V}_\Phi z^{-1} - \hat{H}_{\text{fb}\to\text{in}}(z)\,. \tag{45}$$

The compensated voltage, i.e., the sum of the voltage in Eq. (43) and the voltage from the compensation feedback can be calculated with the help of Fig. 17. In the time domain, it becomes

$$\begin{aligned}
\tilde{v}[n] &= v[n] - \{\hat{V}_\Phi y_{\text{fb}}[n-1] - \hat{h}_{\text{fb}\to\text{in}}[n] * y_{\text{fb}}[n]\} \\
&= V_\Phi x[n] - \hat{V}_\Phi y_{\text{fb}}[n-1] + \{h_{\text{fb}\to\text{in}}[n] - \hat{h}_{\text{fb}\to\text{in}}[n]\} * y_{\text{fb}}[n] \\
&\approx V_\Phi\{x[n] - \Phi_{\text{fb}}[n-1]\}\,,
\end{aligned} \tag{46}$$

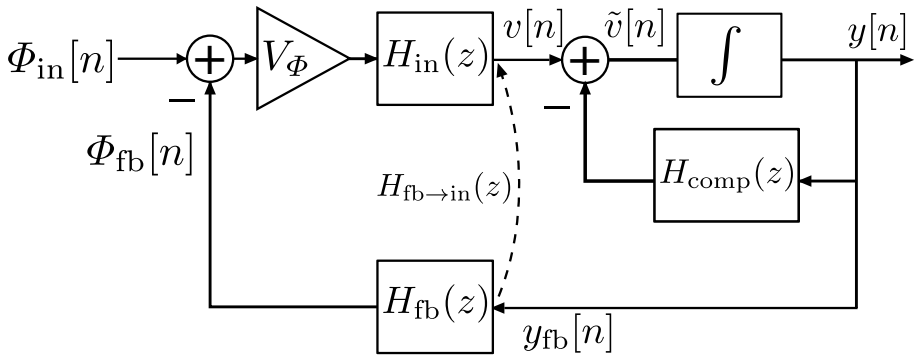

Figure 17: Model for the in-loop-compensated FLL. The integrator element ($\int$) corresponds to a PI controller with $K_\mathrm{P} = 0$.

where the approximation becomes accurate when the estimates correspond to their true values. With perfect compensation, $H_{\mathrm{fb}\to\mathrm{in}}$ does not affect the output of the FLL and the measured flux quantity is $x[n] = (h_{\mathrm{in}} * \Phi_{\mathrm{in}})[n]$, i.e., the input flux affected by the input response.

If the PI input is compensated, the use of a P term in the feedback control becomes pointless, since its only purpose is to speed up the closed-loop response. With $K_\mathrm{P} = 0$, the PI transfer function is $H_\mathrm{PI} = K_\mathrm{I}/(1 - z^{-1})$. The FLL transfer function for the *in-loop-compensated* (ILC) output signal then becomes

$$\begin{aligned} H_{\mathrm{ILC}}(z) = \frac{Y(z)}{X(z)} &= \frac{V_\Phi H_{\mathrm{PI}}(z)}{1 + [H_{\mathrm{fb}\to\mathrm{in}}(z) + H_{\mathrm{comp}}(z)]H_{\mathrm{PI}}(z)} \\ &= \frac{V_\Phi(z)}{(1 - z^{-1})/K_\mathrm{I} + \hat{V}_\Phi z^{-1} + \sum_{n=0}^{N}\{h_{\mathrm{fb}\to\mathrm{in}}[n] - \hat{h}_{\mathrm{fb}\to\mathrm{in}}[n]\}z^{-n}} \\ &= \frac{V_\Phi}{1/K_\mathrm{I} + (\hat{V}_\Phi - 1/K_\mathrm{I})z^{-1} + \Delta H_{\mathrm{fb}\to\mathrm{in}}(z)}\,, \end{aligned} \tag{47}$$

where $\Delta H_{\mathrm{fb}\to\mathrm{in}}(z) = \sum_{n=0}^{N}\{h_{\mathrm{fb}\to\mathrm{in}}[n] - \hat{h}_{\mathrm{fb}\to\mathrm{in}}[n]\}z^{-n}$ is a transfer function that originates from the error in the estimated feedback response. It is easy to see that when $\Delta H_{\mathrm{fb}\to\mathrm{in}}(z) = 0$ and $\hat{V}_\Phi = 1/K_\mathrm{I} = V_\Phi$, the transfer function is one for all z. However, there is always error in the estimates and non-idealities in the system so that, at least for high frequencies, a flat response can be difficult to achieve.

In practice, the compensation is implemented in real-time by convolving the output signal $y[n] = y_{\mathrm{fb}}[n]$ with $h_{\mathrm{comp}}[n]$. The impulse response $h_{\mathrm{comp}}[n]$ is truncated to the first 10 coefficients, thus leaving out the coefficients that are close to zero.

An additional possibility is to use the voltage signal $v[n]$ to compensate the FLL output. Inverting Eq. (43) gives

$$x[n] = \frac{1}{V_\Phi}\{h_{\mathrm{fb}\to\mathrm{in}}[n] * y_{\mathrm{fb}}[n] + v[n]\}\,. \tag{48}$$

Substituting $\hat{h}_{\mathrm{fb}\to\mathrm{in}}[n]$ for $h_{\mathrm{fb}\to\mathrm{in}}[n]$ and $\hat{V}_\Phi$ for V_Φ yields a formula for the *post-loop-*

compensated (PLC) signal

$$y_{\mathrm{PLC}}[n] = \frac{1}{\hat{V}_{\Phi}}\{\hat{h}_{\mathrm{fb}\to\mathrm{in}}[n] * y_{\mathrm{fb}}[n] + v[n]\}. \tag{49}$$

Using Eqs. (43) and (49), the transfer function of the post-loop-compensated system becomes

$$\begin{aligned} H_{\mathrm{PLC}}(z) &= \frac{Y_{\mathrm{PLC}}(z)}{X(z)} \\ &= \frac{1}{\hat{V}_{\Phi}}\{\hat{H}_{\mathrm{fb}\to\mathrm{in}}(z)H_{\mathrm{FLL}}(z) + [V_{\Phi} - H_{\mathrm{fb}\to\mathrm{in}}(z)H_{\mathrm{FLL}}(z)]\} \\ &= \frac{1}{\hat{V}_{\Phi}}\left[\Delta H_{\mathrm{fb}\to\mathrm{in}}(z)H_{\mathrm{FLL}}(z) + V_{\Phi}\right] , \end{aligned} \tag{50}$$

where $H_{\mathrm{FLL}}(z)$ is the FLL transfer function with an ordinary PI feedback.

To eliminate the effect from the input, the compensated signal in both methods should still be deconvolved by an estimate for $h_{\mathrm{in}}[n]$, which recovers the error in the frequency domain up to some frequency. Due to the lack of phase information in the input response measurement, the estimation of the full input impulse response is not possible. Hence, measurements with an externally applied signal are required to fully recover applied the flux.

The main advantage of the post-loop compensation is that its performance does not depend on the integrator gain. The input flux could in theory be recovered up to the accuracy of $\hat{h}_{\mathrm{fb}\to\mathrm{in}}[n]$. On the downside, the post-loop compensation does not speed up the feedback. Towards higher frequencies, the working point starts to fluctuate, which possibly increases the cross-talk between channels. In-loop compensation stabilizes the working point, which improves the measurements at higher frequencies.

It is also possible to use the both compensation methods at the same time. Although the correctness of the estimates $\hat{h}_{\mathrm{fb}\to\mathrm{in}}[n]$ and $\hat{V}_{\Phi}$ affects both $H_{\mathrm{ILC}}(z)$ [Eq. (47)] and $H_{\mathrm{PLC}}(z)$ [Eq. (50)], the quality of the in-loop-compensated signal should improve with an additional post-loop compensation if the errors in the estimates are small. Furthermore, when the integrator gain K_{I} in an in-loop-compensated FLL is not set accurately to $K_{\mathrm{I}} = 1/V_{\Phi}$, there will be information in the voltage signal $v[n]$, which can be recovered by post-loop-compensation.

4 Results

Feedback-to-input responses $H_{\mathrm{fb}\to\mathrm{in}}(z)$ and input responses $H_{\mathrm{in}}(z)$ were measured for different channels in the MEG–MRI system. The results from these measurements are presented and discussed in Secs. 4.1 and 4.2. The measured feedback responses were used to calculate transfer functions for the FLL with different feedback configurations. The transfer functions are shown in Sec. 4.3. These results are based on the model introduced in Sec. 3.2. Finally, some results of the smart reset algorithm are described in Sec. 4.4.

4.1 Feedback-to-input responses

The feedback-to-input responses $H_{\mathrm{fb}\to\mathrm{in}}(z)$ were measured as described in Sec. 3.4.2. Sinusoids of 10 different frequencies were applied to the feedback, and the input signals were measured using quadrature detection. Each of the frequencies were measured 20 times for averaging. The feedback responses of two different channels in the frequency and time domains are shown in Figs. 18 and 19. These channels were chosen as examples to demonstrate differences between two families of responses, to which most of the measured channels belonged. One magnetometer and one gradiometer was chosen to show differences in the measurement error between the two pickup types.

In Figs. 18a and 19a, data from the frequency response measurements are shown. The dots mark the means, and the error bars represent the standard deviations over the 20 samples. From the frequency response data, we can see that the responses have low-pass characteristics with nearly linear phase responses. The gain response of the magnetometer in the first family (Fig. 18a) is clearly non-zero close to the Nyquist frequency, whereas the high-frequency response of the gradiometer in the second family (Fig. 19a) is much closer to zero. The slope of the phase response of the second family is somewhat steeper than that of the first, which indicates a longer delay. In the magnetometer channels, the standard deviations were usually larger because of external field fluctuations. In the gradiometer channels, the standard deviations were negligible.

The discrete Fourier transform was used to calculate the impulse responses $h_{\mathrm{fb}\to\mathrm{in}}[n]$. The conversion to the time domain was motivated by the compensation methods, which utilize the impulse response (Sec. 3.4.5). Differences in the responses can also be seen in the time domain: the first family had a dead time of 2 samples and an average delay of 3.6 samples; for the second family, the numbers were 3 samples and 4.4 samples, respectively. Examples of these impulse response types are plotted in Figs. 18b and 19b. The ideal feedback impulse response $V_\Phi\delta[n-1]$ is a unit-delay response with a channel-specific gain. The additional delay in $h_{\mathrm{fb}\to\mathrm{in}}[n]$ degrades the FLL closed-loop response, as shown in Sec. 4.3.

After normalizing the responses by $\hat{V}_\Phi$, the differences between the responses within the families were smaller than between the families, as shown in Appendix A. Only two of the 32 measured channels showed a response different from the main families. The differences originate most probably from dissimilarities in the analog

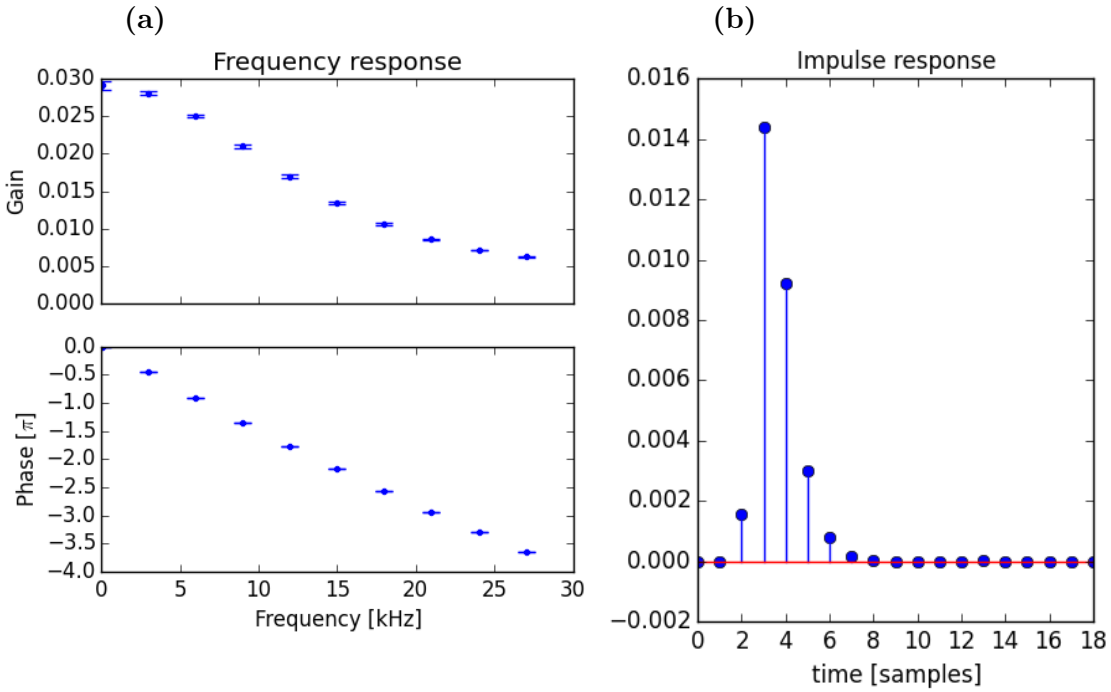

Figure 18: The feedback response $H_{\text{fb}\to\text{in}}$ of a magnetometer (MEG2111) from the first family of responses.

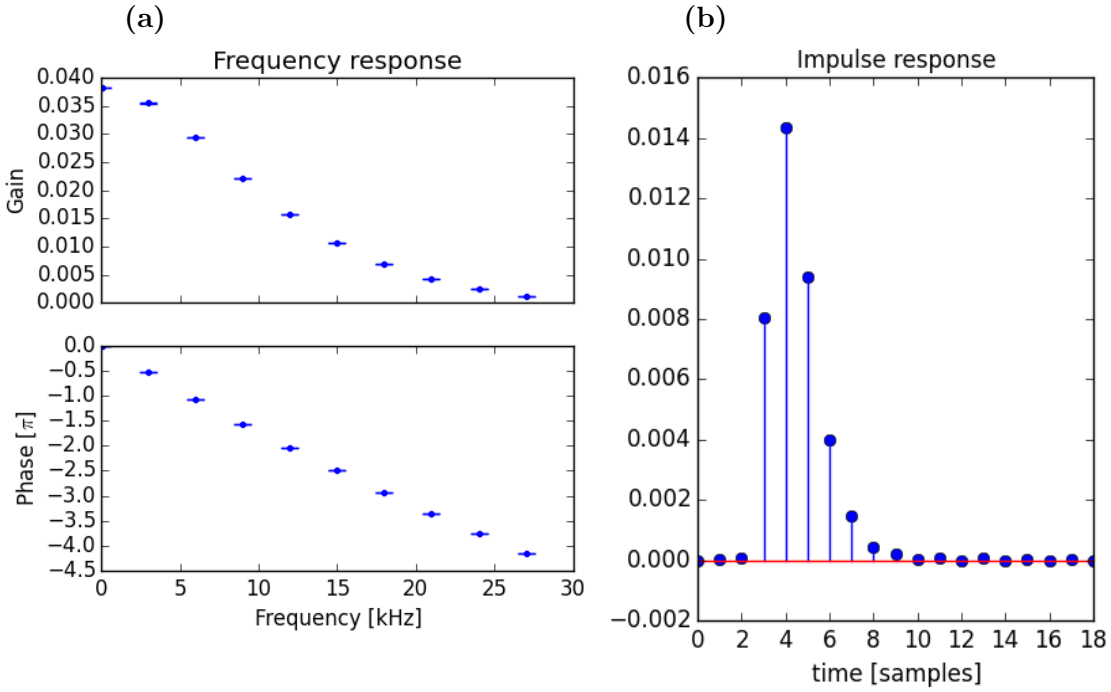

Figure 19: The feedback response $H_{\text{fb}\to\text{in}}$ of a gradiometer (MEG1412) from the second family of responses.

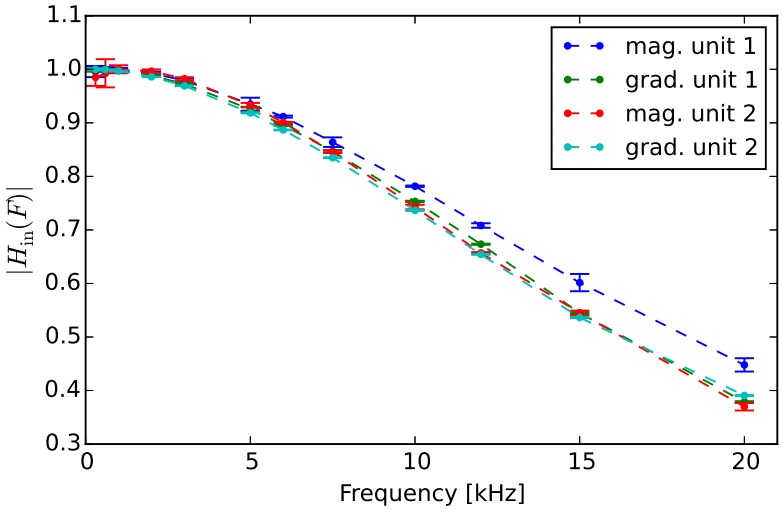

Figure 20: Input frequency responses $|H_{\mathrm{in}}(F)|$ of four different channels (MEG2111, MEG2112, MEG1411, and MEG1412).

signal filtering. Another reason can be a difference in data transfer delays.

4.2 Input frequency responses

The input responses were measured as described in Sec. 3.4.3. The main idea was to use the SQUID transfer function as a periodic excitation signal for the input system. To demonstrate the operation of the method, a few channels were measured. The gain responses $|H_{\mathrm{in}}(F)|$ of a magnetometer and a gradiometer from two different sensor units are shown in Fig. 20. Again, the error bars depict standard deviations over 20 measurements, the dots showing the mean values.

The magnetometer measurements are more noisy because of the higher sensitivity to the external field. Furthermore, the magnetometer channels show a slight decrease in the response towards DC. This could be some bias effect in the response measurement due to the external flux noise, which increases at low frequencies and affects the phase of the SQUID output. The low-frequency noise could change the effective frequency of the wave and thus decrease the peak height at the measured frequency.

All channels, apart from the magnetometer of sensor unit 1, show a nearly identical roll-off towards high frequencies. For this magnetometer, the roll-off is clearly milder above 5 kHz. More investigations are required to determine whether this is only an artifact in the measurement of the specific channel.

The data show that the input response starts to roll off below 5 kHz. The typical Larmor frequency in ULF MRI is 2–3 kHz and the measurement bandwidth is about 500–1000 Hz. For those frequencies, the input frequency response is reasonably flat. However, to acquire MRI signal at a higher B_0, the roll-off in the input response should be taken into account. From 5 to 20 kHz the decrease in the response seems almost linear, the total decrease being about 60%. As an example, over a 1-kHz band centered at 10 kHz, the decrease in signal amplitude is about 5 %.

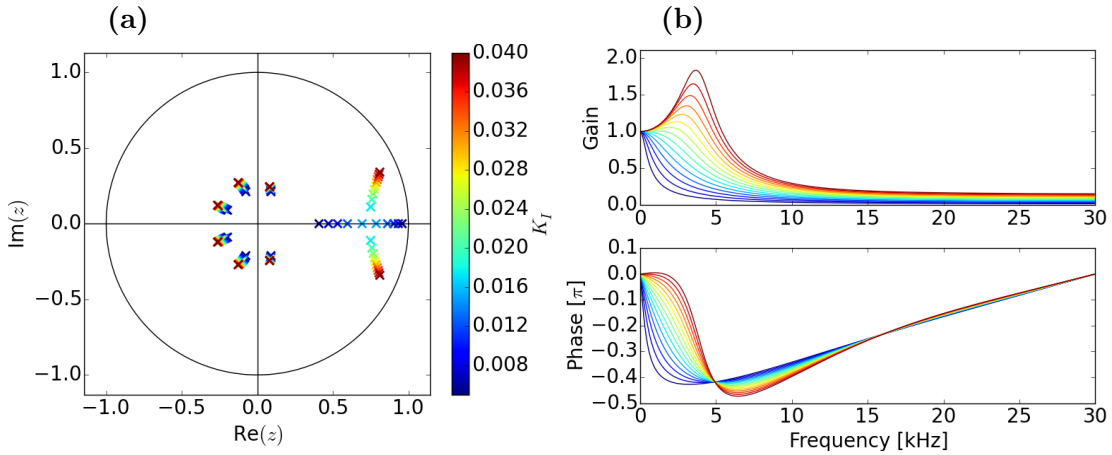

Figure 21: FLL response with integrator feedback, $K_\mathrm{P} = 0$. The values of the integrator gain K_I are shown in the color bar.

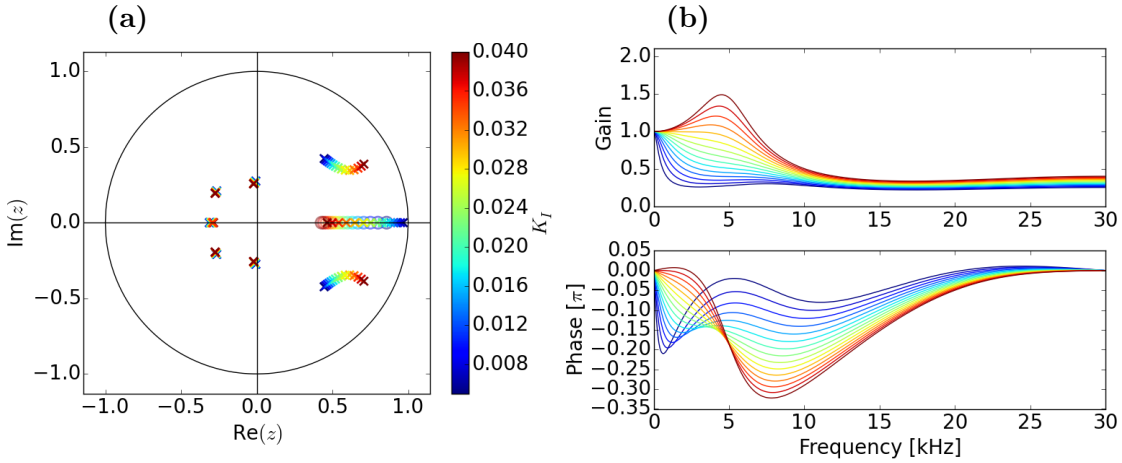

Figure 22: FLL response with PI feedback $K_\mathrm{P} = 0.03$. The zeros are depicted as rings on the real axis. The values of the integrator gain K_I are shown in the color bar.

4.3 Closed-loop frequency responses

In this section, I present examples of FLL closed-loop responses for different feedback implementations. The responses were calculated using the impulse response $h_{\mathrm{fb}\to\mathrm{in}}[n]$ shown in Fig. 18b. Eq. (31) was used to calculate responses of FLLs with an integrator and those with a PI feedback. In addition, responses of an in-loop-compensated FLL were calculated according to Eq. (47). The poles of the transfer function are plotted in the left subfigures of Figs. 21–24, with colors corresponding to the different integrator gains. The right subfigures plot groups of frequency responses $H_\mathrm{FLL}(F)$, also colored based on the integrator gain.

As a reminder, the figures describe the responses of the digital output $y[n]$ to the input-affected flux signal $x[n] = (h_{\mathrm{in,a}} * \Phi_{\mathrm{in,a}})[n]$. In order to get a better

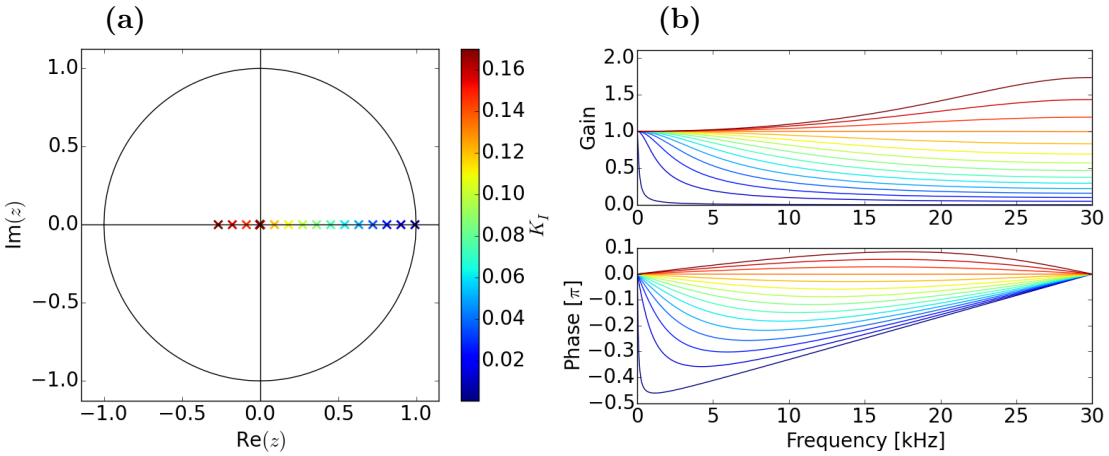

Figure 23: FLL response with ideal feedback compensation. The frequency response can be made flat by choosing an optimal integrator gain. The values of the integrator gain K_I are shown in the color bar.

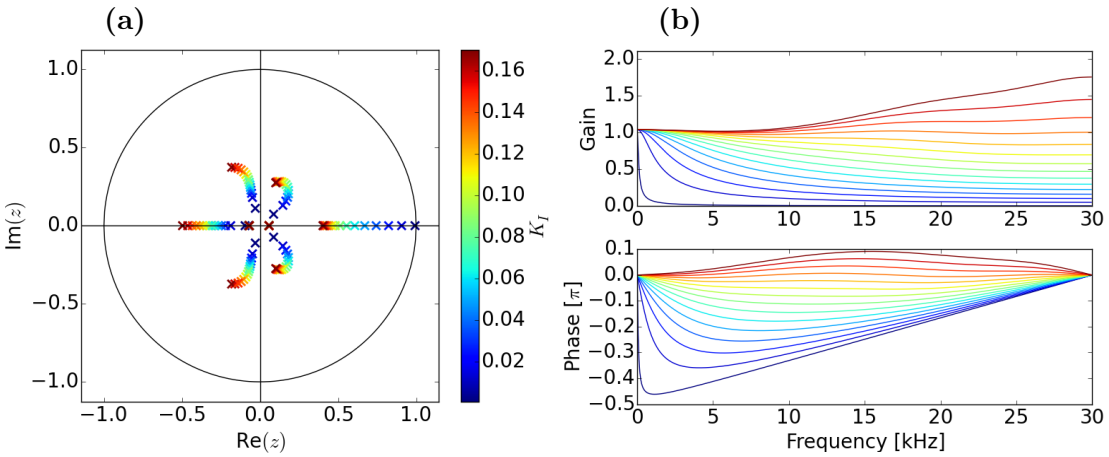

Figure 24: FLL response with more realistic feedback compensation. The errors in the transfer function coefficients cause additional poles, which slightly affect the frequency response. The values of the integrator gain K_I are shown in the color bar.

representation of the flux $\Phi_\mathrm{in}[n]$ at the sampling instants, the output signal $y[n]$ should still be compensated for the effect of $h_\mathrm{in,a}(t)$.

The responses of an integrator FLL ($K_\mathrm{P} = 0$) and a PI FLL with $K_\mathrm{P} = 0.03$ are shown in Fig. 21 and Fig. 22, respectively. Both responses contain conjugate poles that approach the unit circle as the integrator gain is increased. In the PI FLL, the poles cause resonance slightly above 5 kHz, whereas in the integrator FLL, the poles approach the unit circle at frequencies below 5 kHz. As mentioned in Sec. 3.2, the proportional gain also adds a zero to the transfer function. This zero is, however, compensated for with a pole that is always close to it on the real axis, as shown in Fig. 22.

The pole locations determine the shape of frequency response. As the poles in the PI FLL are more broadly distributed than in the pure integrator FLL, the flat part of the frequency response can be further extended, up to 4–5 kHz, with an optimal integrator gain (orange curve in Fig. 22b). The proportional gain K_P also affects the response and the optimum was found to be 0.03 by visual inspection. When a mere integrator is used, the conjugate poles approach the unit circle much faster with increasing K_I. In consequence, the optimally flat frequency response (green curve in Fig. 21b) extends only up to 2–3 kHz, since setting K_I even higher causes resonance.

Figures 23 and 24 show the responses of in-loop-compensated FLLs, colored based on the integrator gain K_I. Fig. 23 plots the case of ideal compensation, where the measured impulse response $\hat{h}_{\mathrm{fb}\to\mathrm{in}}[n]$ exactly matches the true response; $\hat{h}_{\mathrm{fb}\to\mathrm{in}}[n] = h_{\mathrm{fb}\to\mathrm{in}}[n]$. In consequence, the effective feedback is the signal applied to the DAC with a unit delay $V_\Phi y_\mathrm{fb}[n-1]$, as stated approximately by Eq. (46). When the integrator gain is chosen correctly (orange curve in Fig. 23b), the feedback follows the input-affected applied flux perfectly, and the frequency response is flat.

In practice, such a situation can be difficult to achieve. A more realistic case is depicted in Fig. 24, where $\hat{h}_{\mathrm{fb}\to\mathrm{in}}[n]$ differs from $h_{\mathrm{fb}\to\mathrm{in}}[n]$. The error terms $h_{\mathrm{fb}\to\mathrm{in}}[n] - \hat{h}_{\mathrm{fb}\to\mathrm{in}}[n]$ in Eq. (47) were simulated using Gaussian random numbers with standard deviations of $0.05\hat{h}_{\mathrm{fb}\to\mathrm{in}}[n]$. The inaccurate impulse response generates poles, the locations of which are functions of the error terms. As expected, it was found that, the larger the error, the further from the origin the poles move as the integrator gain is increased. Fortunately, the system is not too sensitive to the errors. For example, in Fig. 24, the influence of the additional poles on the frequency response is not very significant. However, in practice, there may be some additional non-idealities that deteriorate the response.

4.4 Smart reset

The reset algorithm described in Sec. 3.3 was implemented on the DSP units. The total duration of the algorithm phases from the initial flux swing (phase 1) to switch on the FLL (phase 7) was squeezed under one millisecond. Experimental evidence of the effect of the initial flux swing to the operation of the flux dams was not yet obtained, but at least the algorithm worked expectedly in normal conditions. Some problems in the program execution were encountered when many SQUIDs were reset simultaneously. These were, however, solved by simplifying the reset triggering, lightening the executed code, and synchronizing the FLL switch-on across different sensors.

An example of reset control in the absence of external transient magnetic fields was already shown in Fig. 12. The displacement from the working point can be seen as a small offset in the SQUID voltage before the FLL is switched on. In flux, this error typically corresponded to 1% of Φ_0. In harsher conditions, where the external field is changing nonlinearly, it may be larger. The feedback compensation for linearly changing input flux was shown to work in computer simulations.

Fig. 25 shows an example of the effect of smart reset on the decimated SQUID signal acquired on the measurement computer. The signal levels at 4 ms were shifted

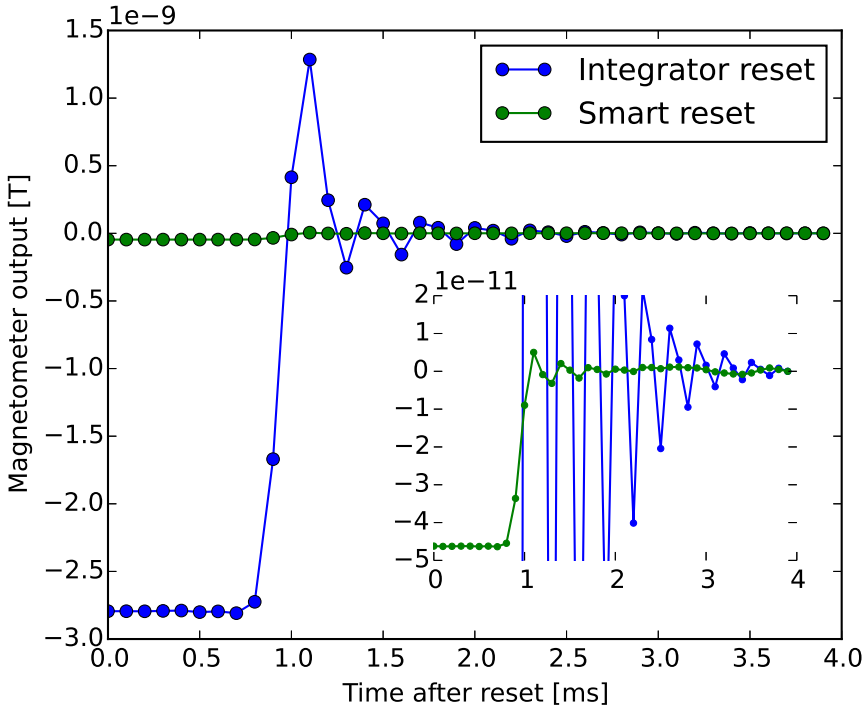

Figure 25: Examples of data acquired at 10 kHz after the reset at 0 ms. The inner figure is a close-up near 0 T.

to zero to make the plots comparable. The reset phases finished approximately at 0 ms. After one millisecond, the traditional reset shows a 100-fold transient compared to the smart reset algorithm. In the smart reset, the filter states are initialized close to the new output value and, hence, the transient is suppressed.

When comparing the reset signals to the step response of the FIR–IIR decimation filter in Appendix B, it becomes clear that the reason for the transient is the filter. In the case of smart reset, the waveform is nearly identical to the filter step response. In the integrator reset, the initial peak in the step response relative to the height of the step is somewhat larger than in the smart reset response (compare the points at 1 ms). This most probably originates from the feedback drift before the FLL locks, as shown in Fig. 10, where the drift lasts for 0.5 ms. The transient from the locking is, however, much faster than the filter transient since the DSP loop runs at 60 kHz, whereas the IIR part of the decimation filter is applied at 10 kHz.

In fact, a large part of the step transient originates from the IIR filter. As shown in Appendix B, the step response of the FIR filter converges to unity in two milliseconds, whereas the convergence of the combined FIR–IIR filter is much slower. A short settling time is crucial for getting proper signals, because the detected ULF MRI signals are extremely small, and any interference from the filter transient can disturb them. In conclusion, the IIR filter could be bypassed and the decimation filtering for the 10-kHz sampling rate should be performed using only the FIR filter.

5 Conclusions

In this thesis, the DSP control of SQUID magnetometers for ultra-low-field magnetic resonance was studied and improved. The software containing a digital flux-locked loop, originally designed for MEG, was used as a basis for the work. It was extended with additional functionality to enable the measurement of the system parameters and efficient feedback flux control during ULF MRI data acquisition.

After characterizing the system, a new FLL reset algorithm for ULF MRI was developed. Issues in the old FLL reset included unpredictable operation of the flux dams in the SQUID input circuit and long transients after flux locking. The new reset algorithm contains a flux swing to wake up the flux dams and a method to quickly locate a suitable FLL working point while affected by a drift in the external flux.

In addition, the decimation filters were found to be an issue, since they produce a large transient signal after resetting the FLL. The transient mainly originates from the large DC step in the FLL output signal and can be attenuated by initializing the filter state to correspond to the new feedback flux. Favoring an FIR filter over an IIR filter in the decimation also reduces the transient time.

The FLL frequency responses were analyzed using a discrete-time model for the feedback loop. Non-idealities of the feedback and voltage input were studied by applying sinusoidal signals to the feedback and measuring them in the voltage input. The sampled frequency response was transformed into an impulse response using the discrete Fourier transform. The experimental feedback-to-input impulse response was used in the model, which enabled the calculation of the transfer function of the FLL closed-loop response.

The average delay in the feedback was measured to be 3–4 samples, which corresponds to 50–70 µs at a 60-kHz sampling rate. Because of this, the closed-loop frequency response of the system rolls off at 3 kHz when using integrator feedback. The frequency response can be extended by 1–2 kHz by adding an optimized proportional gain parallel to the integrator. The PI-controlled feedback, which was already implemented in the original software, is well suited for MEG, which measures relatively low-frequency signals.

For ULF MRI, a better frequency response would enable the use of a somewhat higher B_0. It was shown that the FLL frequency response can be improved when taking into account the suboptimal feedback and input responses. The closed-loop response can be improved by implementing an additional digital in-loop compensation feedback to the FLL software. Alternatively, the signal loss in the FLL output can be post-loop compensated using the SQUID voltage signal.

Compensating the FLL digitally could, in theory, extend the usable frequency range close to the Nyquist frequency. In practice, non-idealities that are not modeled in the feedback loop may become an issue at much lower frequencies. Furthermore, cross-talk between the different sensors may become an issue at high frequencies, where the feedback does not properly follow the applied signal. Even if the feedback is perfectly compensated on the DSP, the signal is always filtered by the D/A electronics before it is applied to the SQUID. Despite these issues, it may be possible to increase

the flat part of the frequency response by 5–10 kHz. Finally, the input response has to be taken into account to fully compensate the signal, since the roll-off affects fairly low frequencies.

Although the FLL frequency response can be improved digitally, an easier solution for measuring higher frequencies would be faster hardware. Speeding up the feedback response might require replacing the DSP units with another technology at least for the FLL calculations. To increase the dynamic range of the system, the flux-quantum-counting method could be implemented.

A faster feedback loop would also allow a faster reset. The FLL transient time would substantially decrease and the flux swing could be carried out without additional waiting. Also, the FLL settling time from non-zero voltage to a stable working point would not be an issue. However, when the FLL runs at a very high sampling rate, the output signal requires decimation before being sent for recording and analysis. Hence, the decimation filter still needs to be reset in conjunction with the FLL to reduce the transient in the decimated signal.

In summary, this work has addressed problems in digital signal acquisition and control of the SQUID sensors for ULF MRI. The smart reset algorithm can reduce the waiting time after the field pulses in the imaging sequence and lead to more reliable operation of the sensors after the reset. Thanks to the characterization of the voltage input and feedback responses, digital compensation of the hardware non-idealities could be implemented to enable measurements at higher frequencies.

References

[1] E. M. Haacke, R. W. Brown, M. R. Thompson, and R. Venkatesan. *Magnetic Resonance Imaging: Physical Principles and Sequence Design*. John Wiley & Sons, 1999.

[2] Z.-P. Liang and P. C. Lauterbur. *Principles of magnetic resonance imaging*. SPIE Optical Engineering Press, 2000.

[3] J. Clarke, M. Hatridge, and M. Mößle. "SQUID-Detected Magnetic Resonance Imaging in Microtesla Fields". *Annual Review of Biomedical Engineering* 9.1 (2007), pp. 389–413.

[4] M. Hämäläinen, R. Hari, R. J. Ilmoniemi, J. Knuutila, and O. Lounasmaa. "Magnetoencephalography—theory, instrumentation, and applications to non-invasive studies of the working human brain". *Reviews of Modern Physics* 65 (1993), pp. 413–497.

[5] J. Clarke and A. I. Braginski, eds. *The SQUID Handbook: Fundamentals and Technology of SQUIDs and SQUID Systems*. First Edition. Wiley-VCH, 2004.

[6] P. T. Vesanen, J. O. Nieminen, K. C. J. Zevenhoven, J. Dabek, L. T. Parkkonen, A. V. Zhdanov, J. Luomahaara, J. Hassel, J. Penttilä, J. Simola, A. I. Ahonen, J. P. Mäkelä, and R. J. Ilmoniemi. "Hybrid ultra-low-field MRI and magnetoencephalography system based on a commercial whole-head neuromagnetometer". *Magnetic Resonance in Medicine* 69.6 (2013), pp. 1795–1804.

[7] R. McDermott, S. Lee, B. Ten Haken, A. H. Trabesinger, A. Pines, and J. Clarke. "Microtesla MRI with a superconducting quantum interference device". *Proceedings of the National Academy of Sciences of the United States of America* 101.21 (2004), pp. 7857–7861.

[8] V. S. Zotev, A. N. Matlashov, P. L. Volegov, A. V. Urbaitis, M. A. Espy, and R. H. Kraus Jr. "SQUID-based instrumentation for ultralow-field MRI". *Superconductor Science and Technology* 20.11 (2007), S367.

[9] M. Mößle, S.-I. Han, W. R. Myers, S.-K. Lee, N. Kelso, M. Hatridge, A. Pines, and J. Clarke. "SQUID-detected microtesla MRI in the presence of metal". *Journal of Magnetic Resonance* 179.1 (2006), pp. 146–151.

[10] S. K. Lee, M. Möβle, W. Myers, N. Kelso, A. H. Trabesinger, A. Pines, and J. Clarke. "SQUID-detected MRI at 132 μT with T1-weighted contrast established at 10 μT–300 mT". *Magnetic Resonance in Medicine* 53.1 (2005), pp. 9–14.

[11] P. T. Vesanen, J. O. Nieminen, K. C. J. Zevenhoven, Y.-C. Hsu, and R. J. Ilmoniemi. "Current-density imaging using ultra-low-field MRI with zero-field encoding". *Magnetic Resonance Imaging* 32.6 (2014), pp. 766–770.

[12] Y. S. Greenberg. "Application of superconducting quantum interference devices to nuclear magnetic resonance". *Reviews of Modern Physics* 70 (1998), pp. 175–222.

[13] J. Luomahaara, P. T. Vesanen, J. Penttilä, J. O. Nieminen, J. Dabek, J. Simola, M. Kiviranta, L. Grönberg, C. J. Zevenhoven, R. J. Ilmoniemi, et al. "All-planar SQUIDs and pickup coils for combined MEG and MRI". *Superconductor Science and Technology* 24.7 (2011), p. 075020.

[14] P. T. Vesanen, J. O. Nieminen, K. C. J. Zevenhoven, J. Dabek, J. Simola, J. Sarvas, and R. J. Ilmoniemi. "The spatial and temporal distortion of magnetic fields applied inside a magnetically shielded room". *IEEE Transactions on Magnetics* 48.1 (2012), pp. 53–61.

[15] J. O. Nieminen, P. T. Vesanen, K. C. J. Zevenhoven, J. Dabek, J. Hassel, J. Luomahaara, J. S. Penttilä, and R. J. Ilmoniemi. "Avoiding eddy-current problems in ultra-low-field MRI with self-shielded polarizing coils". *Journal of Magnetic Resonance* 212.1 (2011), pp. 154–160.

[16] K. C. J. Zevenhoven, H. Dong, R. J. Ilmoniemi, and J. Clarke. "Dynamical cancellation of pulse-induced transients in a metallic shielded room for ultra-low-field magnetic resonance imaging". *Applied Physics Letters* 106.3 (2015), p. 034101.

[17] V. S. Zotev, A. N. Matlashov, P. L. Volegov, I. M. Savukov, M. A. Espy, J. C. Mosher, J. J. Gomez, and R. H. Kraus Jr. "Microtesla MRI of the human brain combined with MEG". *Journal of Magnetic Resonance* 194.1 (2008), pp. 115–120.

[18] V. Pizzella, S. Della Penna, C. Del Gratta, and G. L. Romani. "SQUID systems for biomagnetic imaging". *Superconductor Science and Technology* 14.7 (2001), R79.

[19] A. Mäkinen. *A novel method for fully automatic co-registration of MEG and ULF MRI.* Special assignment. Aalto University, 2015.

[20] T. Orlando and K. A. Delin. *Foundations of Applied Superconductivity.* Prentice Hall, 1991.

[21] F. Schwabl. *Quantum Mechanics.* Third Edition. Springer-Verlag, 2002.

[22] R. Feynman, R. Leighton, and M. Sands. *The Feynman Lectures on Physics.* Second Edition. Vol. 3. Addison-Wesley, 1964.

[23] A. Barone and G. Paternò. *Physics and applications of the Josephson effect.* Wiley, 1982.

[24] D. Drung. "Advanced SQUID read-out electronics". In: *SQUID Sensors: Fundamentals, Fabrication and Applications.* Springer, 1996, pp. 63–116.

[25] M. Kajola, ed. *Sensor Tuner User's Guide.* Elekta Neuromag, 2009.

[26] M. Kiviranta and H. Seppä. "DC-SQUID electronics based on the noise cancellation scheme". *IEEE Transactions on Applied Superconductivity* 5.2 (1995), pp. 2146–2148.

[27] H. J. M. Ter Brake, F. H. Fleuren, J. A. Ulfrnan, and J. Flokstra. "Elimination of flux-transformer crosstalk in multichannel SQUID magnetometers". *Cryogenics* 26.12 (1986), pp. 667–670.

[28] J. McKay, J. Vrba, K. Betts, M. Burbank, S. Lee, K. Mori, D. Nonis, P. Spear, and Y. Uriel. "Implementation of a multi-channel biomagnetic measurement system using DSP technology". In: *Canadian Conference on Electrical and Computer Engineering*. IEEE. 1993, pp. 1090–1093.

[29] R. R. Bracht, P.-J. Kung, P. S. Lewis, and E. R. Flynn. *DSP control of superconducting quantum interference devices*. Tech. rep. Los Alamos National Lab., NM (United States), 1994.

[30] E. R. Flynn, R. Bracht, R. H. Kraus Jr., P. M. Maas, P. Ruminer, and M. Stettler. "A Digital-Signal-Processor (DSP) Flux-Locked-Loop (FLL) for LTC SQUIDs with Automatic Reset and Feedback Cancellation". In: *Biomag 96: Proceedings of the Tenth International Conference on Biomagnetism*. Springer, 2000, pp. 39–42.

[31] C. Ludwig, C. Kessler, A. Steinforc, and W. Ludwig. "Versatile high performance digital SQUID electronics". *IEEE Transactions on Applied Superconductivity* 11.1 (2001), pp. 1122–1125.

[32] D. Oyama, K. Kobayashi, M. Yoshizawa, and Y. Uchikawa. "Development of Digital FLL System for SQUID Using Double Counter Method". *IEEE Transactions on Magnetics* 42.10 (2006), pp. 3539–3541.

[33] J. G. Proakis and D. K. Manolakis. *Digital Signal Processing (4th Edition)*. Prentice-Hall, Inc., 2006.

[34] K. J. Åström and B. Wittenmark. *Computer-controlled Systems: Theory and Design*. Prentice-Hall, Inc., 1984.

[35] R. H. Koch, J. Z. Sun, V. Foglietti, and W. J. Gallagher. "Flux dam, a method to reduce extra low frequency noise when a superconducting magnetometer is exposed to a magnetic field". *Applied Physics Letters* 67.5 (1995), pp. 709–711.

A Feedback-to-input impulse responses and delays

The sampled frequency responses $H_{\mathrm{fb}\to\mathrm{in}}(F)$ of 32 different channels were measured. These measurements were converted to impulse responses $h_{\mathrm{fb}\to\mathrm{in}}[n]$ as described in Sec. 3.4.2. In Fig. A1, normalized impulse responses ($\sum_n h_{\mathrm{fb}\to\mathrm{in}}[n] = 1$) of the 32 channels are plotted. The responses mainly divide in two different families, which are plotted in blue and green; two outlier channels are plotted in red and yellow. The average delays in the feedback signals are calculated as

$$d = \sum_{n=0}^{N-1} h_{\mathrm{fb}\to\mathrm{in}}[n]\, n\,, \tag{A1}$$

and plotted as histogram in Fig. A2.

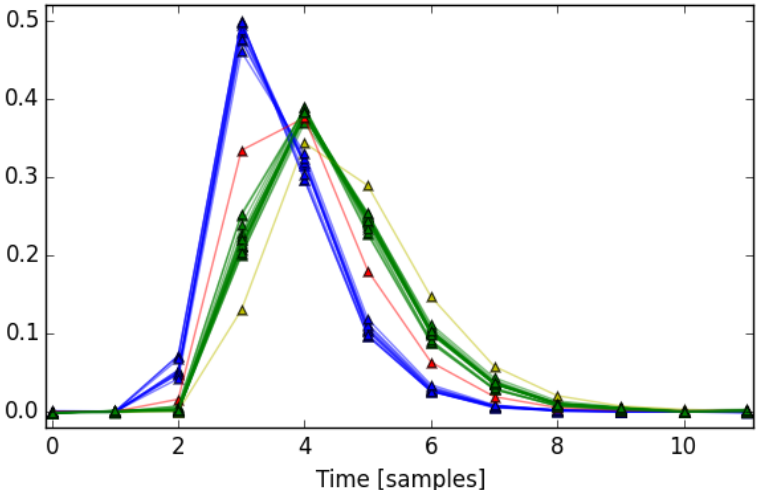

Figure A1: Normalized impulse responses. The samples in each response are connected by straight lines.

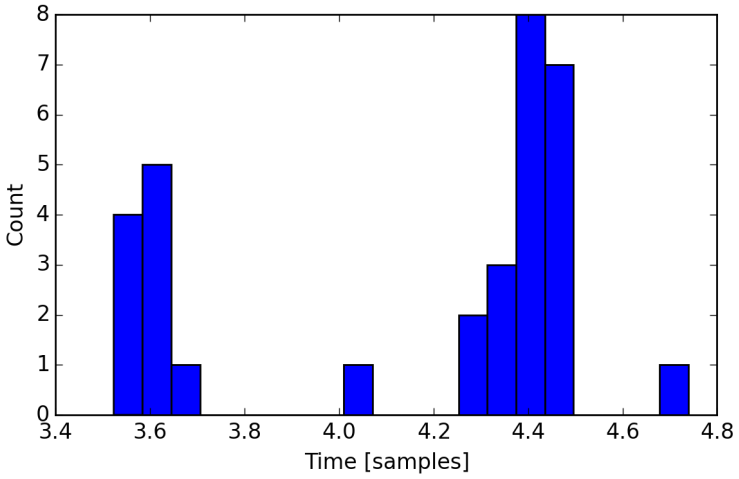

Figure A2: Histogram of average delays in the feedback signals.

B Decimation filters

After resetting the FLL integrator, it is vital to reset also the decimation filter states to reduce their step transient. The decimation filter is a combined FIR–IIR filter, as described in Sec. 3.1.

The memory of the FIR filter consists of previous inputs $x[n-k]$, where $0 < k \leq 128$. These values are set to the new feedback signal value $y_{\mathrm{fb},0}$ that is assumed to be close to the new working point value $y_{\mathrm{fb,W}}$. In consequence, the FIR filter will only experience a step of $y_{\mathrm{fb,W}} - y_{\mathrm{fb},0}$ which is presumably at least 100–1000 times smaller than without initializing the filter state.

Resetting the IIR filter is somewhat more complicated. The filter comprises three cascaded second-order IIR filters implemented in direct form II (DFII). Each subsystem can be written as

$$\begin{aligned} Y(z) = H(z)X(z) = \frac{B(z)}{A(z)}X(z) &= \frac{b_0 + b_1 z^{-1} + b_2 z^{-2}}{1 + a_1 z^{-1} + a_2 z^{-2}}X(z) \\ \xRightarrow{\text{DFII}} &\begin{cases} Y(z) = B(z)W(z) \\ W(z) = X(z)/A(z)\,, \end{cases} \end{aligned} \tag{B1}$$

where $X(z)$ is the input to the system, $Y(z)$ the output, and $W(z)$ an intermediate signal. Transforming back to the time domain yields

$$\begin{aligned} y[n] &= b_0 w[n] + b_1 w[n-1] + b_2 w[n-2] \\ w[n] &= x[n] - a_1 w[n-1] - a_2 w[n-2]\,, \end{aligned} \tag{B2}$$

where the memory of the filter are $w[n-1]$ and $w[n-2]$. Assuming that the filter has accommodated to a constant input, $w[n]$ will be the same for all n. If the input is $y_{\mathrm{fb},0}$ and the intermediate signal is denoted as w_∞, the first subsystem can be solved as

$$\begin{aligned} y_\infty &= (b_0 + b_1 + b_2) w_\infty \\ w_\infty &= \frac{y_{\mathrm{fb},0}}{1 + a_1 + a_2}\,. \end{aligned} \tag{B3}$$

Variables $w[n-1]$ and $w[n-2]$ of the first subsystem are set to w_∞, and y_∞ is used as an input for the next subsystem. The same formula with different coefficients is applied to initialize the memories of the next two subsystems. The output of the last subsystem should be the same as the input to the first, which can be used to check the calculations.

The step response of the FIR–IIR filter for decimation from 60 kHz to 10 kHz is shown in Fig. B1. The absolute error compared to the unit step decays quite slowly as a function of time. For comparison, the decimated step response of the mere FIR filter is also shown in Fig. B1. The error compared to the unit step disappears after approximately 2 ms, which is the length of the finite impulse response. The first millisecond in the responses, where nothing notable happens, is actually a delay from the FIR filter. Thus, the effective transient of the FIR filter only lasts for about 1 ms.

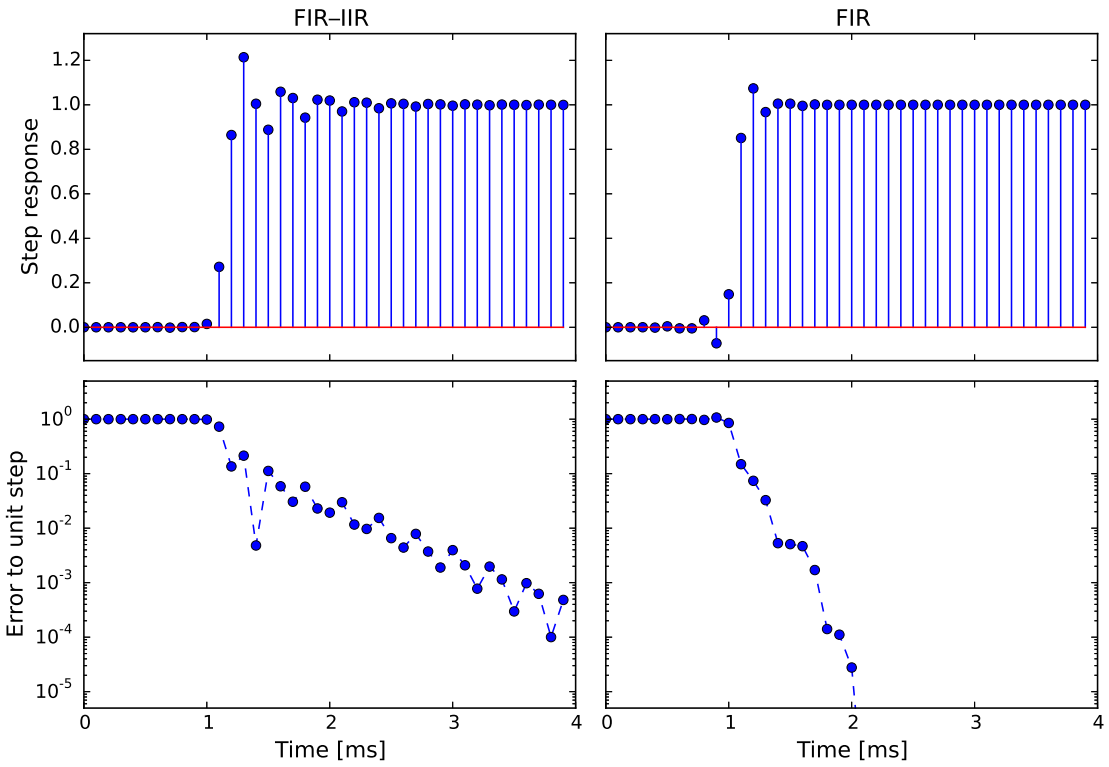

Figure B1: At the top, unit step responses for the combined FIR–IIR filter and the mere FIR filter (after decimation) calculated from the filter transfer functions. At the bottom, the absolute error of the responses compared to unity on a logarithmic scale.